



Van Zalinge, M. E., Sparks, R. S. J., Cooper, F. J., & Condon, D. J. (2016). Early Miocene large-volume ignimbrites of the Oxaya Formation, Central Andes. *Journal of the Geological Society*, 173(5), 716-733. DOI: 10.1144/jgs2015-123

Peer reviewed version

Link to published version (if available):
[10.1144/jgs2015-123](https://doi.org/10.1144/jgs2015-123)

[Link to publication record in Explore Bristol Research](#)
PDF-document

This is the author accepted manuscript (AAM). The final published version (version of record) is available online via the Geological Society at <http://jgs.lyellcollection.org/content/early/2016/03/30/jgs2015-123.abstract>

University of Bristol - Explore Bristol Research

General rights

This document is made available in accordance with publisher policies. Please cite only the published version using the reference above. Full terms of use are available:
<http://www.bristol.ac.uk/pure/about/ebr-terms.html>

1 **Early Miocene large volume ignimbrites of the Oxaya Formation,**
2 **Central Andes**

3

4 Authors: van Zalinge, M.E.^{1*}, Sparks, R.S.J.¹, Cooper, F.J.¹, Condon, D.J.²

5 ¹ School of Earth Sciences, University of Bristol, Wills Memorial Building, Queens

6 Road, Clifton, Bristol, BS8 1RJ, United Kingdom

7 ² British Geological Survey, NERC Isotope Geosciences Facilities, Nicker Hill,

8 Keyworth, Nottingham, NG12 5GG, United Kingdom

9 *m.vanzalinge@bristol.ac.uk

10 words text: 8540

11 words references: 2503

12 words figure captions: 574

13 words table camptions: 82

14

15 Running title: Large volume ignimbrites of the Oxaya Formation

16

17 Supplementary material: U-Pb methodology and complete data tables; ICP-OES

18 and ICP-MS methodology and complete data tables; and detailed stratigraphic

19 description of the Cardones ignimbrite are available at

20 www.geolsoc.org.uk/SUP00000.

21

22 **Abstract**

23 During the early Miocene ignimbrite flare-up, significant parts of the Central
24 Andes (17-20°S) were covered by large-volume ignimbrites. High-precision
25 $^{206}\text{Pb}/^{238}\text{U}$ zircon dates constrain the flare up in northern Chile at ~18°S to a 3
26 million year period, starting with the deposition of the Poconchile ignimbrite at
27 22.736 ± 0.021 Ma. Of four main pulses, the two largest occurred at $21.924 \pm$
28 0.011 Ma and 19.711 ± 0.036 Ma, when the >1000 km³ in volume Cardones and
29 the Oxaya ignimbrites erupted, respectively. The ignimbrites are high-SiO₂
30 rhyolites and show significant heterogeneities in crystal content, mineral
31 proportions and trace-element compositions. The zoned Oxaya ignimbrite
32 implies incremental extraction of a crystal-poor magma overlying a crystal-rich
33 magma. In contrast, petrological and textural heterogeneities in pumice clasts
34 are spread throughout the Cardones ignimbrite and we propose magma mixing
35 caused by destabilization of multiple magma bodies within a magmatic mush
36 system. Distal and medial deposits of the Cardones ignimbrite, with a maximum
37 welded thickness of at least 1000 m, entirely covered the western flank of the
38 Central Andes, which implies infill of a significant topographic relief. Both
39 compaction and welding resulted in a maximum thickness reduction of around
40 30% for the Cardones ignimbrite.

41

42 **Keywords:** ignimbrite, flare-up, Cardones, Oxaya, U-Pb geochronology, Central
43 Andes, Chile

44

45

46 Silicic ignimbrites with volumes exceeding 450 km³ form during large-
47 magnitude ($M > 8$), catastrophic eruptions associated with collapsed calderas
48 (Self, 2006, Miller and Wark, 2008, Geyer and Marti, 2008). These large-volume
49 ignimbrites have been characterised as either: 1) crystal-poor rhyolites that are
50 commonly compositionally zoned or 2) crystal-rich (~50%) dacites that are
51 chemically homogenous and often called monotonous intermediates (e.g.
52 Hildreth, 1981; Bachmann and Bergantz, 2008). Well-studied examples of
53 crystal-poor rhyolitic ignimbrites are the Bishop Tuff (>600 km³) in California,
54 USA (Hildreth, 1979; Hildreth and Wilson, 1997, Hildreth and Wilson, 2007) and
55 the Huckleberry Ridge Tuff (>2500 km³) in Yellowstone, USA (Christiansen
56 2001). Well known examples of crystal-rich ignimbrites include the dacitic Fish
57 Canyon Tuff (>5000 km³) in the San Juan Volcanic Field, USA (Steven and
58 Lipman, 1976, Whitney and Stormer, 1985, Lipman *et al.*, 1997, Bachmann *et al.*,
59 2002, Wotzlaw *et al.*, 2013), the rhyodacitic Cerro Galan ignimbrite (~1000 km³)
60 in Argentina (Sparks *et al.*, 1985, Francis *et al.*, 1989, Wright *et al.*, 2011), and
61 the rhyodacitic Youngest Toba Tuff (~2400 km³) in Indonesia (Chesner and
62 Rose, 1991, Chesner, 1998, Vazquez and Reid, 2004). These ignimbrites typically
63 consist of ash and broken crystals with scarce pumice clasts, lack a basal Plinian
64 fall deposit (Hildreth, 1981, Sparks *et al.*, 1985, Best and Christiansen, 1997) and
65 are thought to be associated with the emplacement of large silicic to
66 intermediate batholiths in subduction zone settings (Lipman and Bachmann,
67 2015).

68 Eruptions of large ignimbrites are commonly clustered in space and time,
69 a feature described as an ignimbrite flare-up. These regional flare-ups can persist
70 for several million years and form extensive ignimbrite provinces. For example,

71 the middle Cenozoic Great Basin flare-up in the western USA resulted in at least a
72 dozen eruptions with each having a volume $>1000 \text{ km}^3$ (Best *et al.* 2009 and
73 references therein). In the Central Andes, the Altiplano-Puna (21-24°) flare-up
74 occurred in the late Miocene to Pleistocene, which created a volcanic area
75 $>50000 \text{ km}^2$ (De Silva, 1989, Lindsay *et al.*, 2001, De Silva *et al.*, 2006). An earlier,
76 less well-known ignimbrite flare-up in the Central Andes occurred during the
77 early Miocene (~25-16 Ma) and affected large parts of southern Peru and
78 northern Chile (17-21°S) (Fig. 1b). Known early Miocene ignimbrite sequences in
79 this area are the Huaylillas Formation (~17°S) (Tosdal *et al.*, 1981), the Oxaya
80 Formation (~18°S) (Salas *et al.* 1966, Wörner *et al.*, 2000, García *et al.*, 2004), the
81 Altos de Pica Formation (~19.50°) (Farías *et al.*, 2005, Blanco *et al.*, 2012), and
82 the Huasco and Tambillo ignimbrites (~20°S) (Gardeweg and Sellés, 2013).

83 To develop insights into the nature of the ignimbrites erupted during this
84 flare-up, and the precursor magmatic systems, we present a study of nine
85 vertical drill holes through the $>1000 \text{ m}$ -thick Oxaya Formation in northernmost
86 Chile (Fig. 1). Here the Oxaya Formation contains a succession of four rhyolitic
87 ignimbrites, which are from oldest to youngest the Poconchile ignimbrite, the
88 Cardones ignimbrite, the Molinos ignimbrite and the Oxaya ignimbrite (García *et al.*
89 *et al.*, 2004). We present detailed drill hole logs in combination with high-precision
90 U-Pb zircon isotope dilution-thermal ionisation mass spectrometry (ID-TIMS)
91 geochronology to establish a temporal framework for the Oxaya Formation.
92 Furthermore, major and trace element analyses of juvenile clasts and bulk
93 ignimbrite compositions place constraints on magmatic processes both prior to
94 and during eruption. These nine drill holes gave us a unique opportunity to study
95 the full thickness of the up to $\sim 1000 \text{ m}$ -thick Cardones ignimbrite, a task that is

96 impractical from field outcrops alone. We provide quantitative constraints on the
97 amount of welding by analyzing fiamme aspect ratios, lithic clast content and
98 bulk rock density throughout the ignimbrite. This allows us to present more
99 accurate thickness estimations of the outflow sheets and in turn evaluate the
100 pre-emplacment topography.

101

102 **Geological Setting**

103 ***The Central Andes***

104 Subduction of the Farallón-Nazca plate beneath the South American continent
105 since the Jurassic has resulted in the formation of the Andean Cordillera (Jordán
106 *et al.*, 1983, Scheuber and Gonzalez, 1999, Martinod *et al.*, 2010). The Central
107 Andes define a bend in the orocline that straddles the border between Chile and
108 Peru. Here, the Central Andes are typically divided into five distinct
109 geomorphological units from west to east: The Coastal Cordillera, the Central
110 Basin, the Precordillera, the Western Cordillera and the Altiplano (Fig. 1c).

111 The Altiplano has a mean elevation of ~3.7 km (Isacks, 1988,
112 Allmendinger *et al.*, 1997, Jordan *et al.*, 2010) and is bounded to the west by the
113 Western Cordillera. The present day volcanic arc has been located in the Western
114 Cordillera since Oligocene times, giving rise to volcanic peaks up to ~6500 m in
115 elevation (Garcia and Hérail, 2005). The ~15 km wide western edge of the
116 Western Cordillera is characterised by a fold and thrust belt. Directly to the west
117 lies the ~30 km wide Precordillera, formed by large-scale monoclines and
118 anticlines (Isacks, 1988, Muñoz and Charrier, 1996, García *et al.*, 2004). Here, the
119 elevation of the Andes steeply increases from less than 2000 m up to ~3900 m
120 and is referred to as the Western Andean Slope. River valleys, such as the Lluta,

121 Azapa, and the Camarones Quebradas, deeply incise the slope. The Precordillera
122 is separated from the Central Basin by the blind, steeply dipping, west-vergent
123 Ausipar thrust (Fig. 1d) (García and Hérail, 2005). The Central Basin is ~45 km
124 wide, less than 2000 m in elevation and has not experienced any overt
125 deformation. West of the Central Basin lies the <1200 m-high, 20 km-wide
126 Coastal Cordillera. However, in the axis of the oroclinal bend, near the city of
127 Arica, this coastal range pinches out entirely.

128

129 ***Study area***

130 The study area is located in northernmost Chile (~18°15') on the Western
131 Andean Slope north of the Lluta Quebrada (Fig. 1d). Here, the rocks can be
132 broadly divided into basement lithologies and a volcanic-sedimentary cover
133 sequence. The basement units, which consist of Jurassic-Cretaceous meta-
134 sediments (Salas *et al.* 1966, García *et al.*, 2004) are intruded by a series of late
135 Cretaceous–Palaeocene (66-54 Ma) tonalites, granodiorites, and granites (e.g.
136 the Lluta batholith) (García *et al.*, 2004), that only crop out in the deeply-incised
137 Quebradas.

138 During a late Eocene – Oligocene tectonic period (Incaic phase) the
139 Precordillera and Western Cordillera were uplifted (Charrier *et al.*, 2013).
140 Deformation resulted in uplift, exhumation and erosion of the Cretaceous-
141 Paleocene intrusive rocks in the Precordillera and Western Cordillera, and
142 sedimentation in the Central Basin, where up to ~500 m of fluvial-alluvial
143 conglomerates and sandstones of the Azapa Formation were deposited (Muñoz
144 and Charrier, 1996, Wörner *et al.*, 2002, García *et al.*, 2004, Garcia and Hérail,
145 2005, Wotzlaw *et al.*, 2011, Charrier *et al.*, 2013). The Incaic phase is

146 contemporaneous with a period of flat-slab subduction (Martinod et al., 2010) at
147 a convergence rate ~ 60 mm/yr (Somoza, 1998) and the cessation of volcanism
148 in northern Chile between ~ 38 Ma and ~ 25 Ma (e.g. Lahsen, 1982,
149 Hammerschmidt *et al.*, 1992). From ~ 26 to 20 Ma, the convergence rate rapidly
150 increased to ~ 150 mm/yr (Somoza, 1998). This change marked the end of flat-
151 slab subduction (Martinod *et al.*, 2010) and coincided with the early Miocene
152 ignimbrite flare-up and thus the deposition of the Oxaya Formation across the
153 Central Basin and the Precordillera. In the Western Cordillera, the Lupica
154 Formation is considered to be the equivalent of the Azapa and Oxaya Formation
155 (Fig. 1d) (García *et al.*, 2011, García *et al.*, 2004).

156 After deposition of the Oxaya Formation the convergence rate decreased
157 to the present rate of ~ 80 mm/yr (Somoza, 1998). In the Precordillera, the
158 sequence deformed into the large-scale Huaylillas and Oxaya anticlines to the
159 north and south of the Lluta Quebrada respectively (Fig. 1d). Folding was
160 contemporaneous with folding and thrusting in the Western Cordillera and
161 movement along the Ausipar thrust (Muñoz and Charrier, 1996, García *et al.*,
162 1996, Wörner *et al.*, 2002, Garcia and Hérail, 2005, Charrier *et al.*, 2013). The
163 resulting uplift produced both erosion and accommodation space in the Huaylas
164 and Copaquilla basins, infilled by clastic sediments of the Huaylas Formation
165 (Fig. 1d) (Wörner *et al.*, 2002, García *et al.*, 2004,).

166

167 ***The Oxaya Formation***

168 The Oxaya Formation was first described by Salas et al. (1996) and has since
169 been studied by Tobar et al. (1968), Christensen et al. (1969), Vogel and Vila

170 (1980), Muñoz and Charrier (1996), García et al. (1996), Garcia et al. (2000) and
171 Wörner et al. 2000 and García et al. (2004).

172 On the Western Andean Slope around the Lluta and Azapa Quebradas the
173 base of the Oxaya Formation is marked by the Poconchile ignimbrite ($^{40}\text{Ar}/^{39}\text{Ar}$
174 sanidine date: 22.27 ± 0.15 Ma (2σ); (Wörner *et al.*, 2000)), which is overlain by
175 the Cardones, Molinos, and Oxaya ignimbrites (García *et al.*, 2004). The top of the
176 sequence, the Oxaya ignimbrite, has been dated at 19.7 ± 0.2 (2σ) Ma ($^{40}\text{Ar}/^{39}\text{Ar}$
177 sanidine: García *et al.*, 2004) and 19.72 ± 0.2 (2σ) Ma ($^{40}\text{Ar}/^{39}\text{Ar}$ sanidine:
178 Wörner et al., 2000) and defines most of the present day surface in the area. The
179 Cardones and Oxaya ignimbrites are the thickest and most widespread
180 throughout the Western Andean Slope. According to García et al. (2004), the
181 Cardones ignimbrite has an areal extend of 4200 km² and an average thickness
182 of 300 m that, when combined, gives a minimum volume of 1260 km³. The
183 source caldera has not been identified, but was most likely located east of the
184 study area, where the volcanic arc was located in the early Miocene (Hampel,
185 2002, Mamani *et al.*, 2010). Garcia et al. (2000) suggested that the source caldera
186 for the Oxaya ignimbrite is most likely located in the Western Cordillera, east of
187 the Oxaya Anticline. This ignimbrite has an estimated areal extent of ~8000 km²
188 and total extra-and intra-caldera volume of ~1500 km³ (Garcia et al., 2000).
189 Medial and distal deposits can be found across the study area with thicknesses
190 varying from 20 to 200 m, which in places consists of two flow units (García *et*
191 *al.*, 2004).

192

193 **Sampling and analysis**

194 ***Drill sites and drill holes***

195 This study centres on nine ~1000 m-deep drill holes along a ~50 km wide
196 orogen-perpendicular transect up the Western Andean Slope in northernmost
197 Chile, deep enough to entirely penetrate both the Oxaya and Azapa Formations.
198 Seven holes (7, 4, 2, 1, 5, 6 and 9) lie along a ~SW-NE transect, perpendicular to
199 the Ausipar fault and the hinge line of the Huaylillas anticline (Fig. 1d). Sites 3
200 and 10 lie off-axis, to the southeast of the main transect.

201 Cores from these drill holes in combination with field observations in the
202 Lluta Quebrada form the basis of our study and allowed us to construct a
203 detailed stratigraphy for the Oxaya Formation. The most accessible field location
204 is the Molinos section (Fig. 2) on the north wall of the Lluta Quebrada, ~10 km
205 southwest of drill hole 7 (“M” on Fig 1d.), which exposes a near-complete section
206 through the Oxaya Formation (Fig. 3a). Samples from this section were used as
207 reference material during core logging and allowed us to extend the cross-
208 section towards the Central Basin. Along each core we recorded colour,
209 crystallinity, average crystal size, types of juvenile and lithic clasts, and any
210 breaks in stratigraphy. The diameter of the cores varied between 4 and 10 cm
211 and core quality and recovery were generally excellent (>95%), with the
212 exception of the top part of most cores and of some non-welded intervals, which
213 were friable. Juvenile and lithic clast counts on the Cardones ignimbrite were
214 carried out on most cores. All measurements were made over a 1 m core interval
215 every 5 m by placing a tape measure along the centre of the core and
216 documenting each clast that intersected the tape measure, recording the number
217 of clasts, lithology, and intersection thickness of each clast. To deal with the large
218 datasets we present the total number of clasts per metre interval. In addition, we
219 present the percentage of the core that contained a specific clast type, this we

220 call the intersection percentage. For example: if the tape measure intersected 5
221 lithic clasts with a total thickness of 100 mm over a 1 metre interval, the lithic
222 intersection percentage (IP_{lit}) would be 10%. The same method can be used to
223 calculate an intersection thickness for juvenile clasts (IP_{juv}).

224 To investigate the loss of porosity in pumice and the bulk ignimbrite
225 during welding and compaction, the aspect ratios (width/height) of 5-10 juvenile
226 clasts (fiamme) were measured every 5 metres throughout the Cardones
227 ignimbrite. In addition, the density of 43 bulk ignimbrite samples and 15 pumice
228 clasts were determined with the hydrostatic weighing technique at room
229 temperature (Muller, 1977). To prevent the samples from absorbing water, they
230 were wrapped in Parafilm® with a known weight and density.

231

232 ***U-Pb geochronology***

233 Seven samples from the Poconchile, Cardones, and Oxaya ignimbrites were
234 selected (sample locations in Fig. 3 and 5) to conduct single-crystal zircon U-Pb
235 ID-TIMS geochronology. The analyses were performed at the NERC Isotope
236 Geosciences Laboratory (NIGL) at the British Geological Survey, Keyworth,
237 United Kingdom following a method similar to the one used by Sahy et al. (2015).
238 This includes a chemical abrasion procedure (Mattinson, 2005) and spiking with
239 the EARTHTIME tracer solution (Condon *et al.*, 2015, McLean *et al.*, 2015). For
240 data reduction and uncertainty propagation, we followed the strategy of Bowring
241 et al. (2011) and McLean et al. (2011). More details about the methods can be
242 found in the supplementary material.

243 Details about data description and selection can be found in the
244 supplementary material. $^{206}\text{Pb}/^{238}\text{U}$ dates presented in this paper are corrected

245 for initial Th disequilibrium, using $\text{Th/U}[\text{magma}] = 3.5 \pm 0.5$. Uncertainties are
246 quoted at the 2σ confidence level unless stated otherwise. Uncertainties are
247 listed as $\pm X/Y/Z$, where X is the analytical uncertainty, while Y and Z include
248 propagated uncertainties for tracer calibration, and respectively tracer
249 calibration and the ^{238}U decay constant uncertainty.

250

251 ***Geochemistry***

252 Major and trace element compositions of 43 Cardones ignimbrite, 7 Molinos
253 ignimbrite and 8 Oxaya ignimbrite samples were determined by inductively
254 coupled plasma-optical emission spectrometry (ICP-OES) and inductively
255 coupled plasma-mass spectrometry (ICP-MS), with a JY Horiba ULTIMA2
256 spectrometer at the Element Analysis Facility, Cardiff University, UK. A similar
257 method to that described by McDonald and Viljoen (2006) was used. Details
258 about the method can be found in supplementary material. Major elements
259 measured by ICP-OES have relative analytical uncertainties at the 2σ confidence
260 level of $\sim 2\%$ for Fe and Na and smaller than 1% for all other elements. Trace
261 elements measured by ICP-MS have relative 2σ uncertainty of $\sim 5\%$. The loss on
262 ignition (LOI) measurements have an uncertainty of $\sim 10\%$.

263

264 **Description of lithologies in drill cores**

265 The Azapa Formation and the Oxaya Formation are the dominant lithologies in
266 the drill core (Fig. 3). The Oxaya Formation comprises five members, which are
267 named, from old to young, the Poconchile ignimbrite, the volcanoclastic member,
268 the Cardones ignimbrite, the Molinos ignimbrite and the Oxaya ignimbrite.

269

270 ***Azapa Formation***

271 The Azapa Formation comprises polymict alternations of greenish coloured
272 sandstone, and both matrix- and clast-supported conglomerates. The
273 conglomerates contain angular to well-rounded intrusive (e.g. granite and
274 granodiorite), volcanic (e.g. dacite and andesite (often altered)), sedimentary
275 (e.g. limestone and sandstone) and minor metamorphic (gneiss and amphibolite)
276 clasts in a sandy matrix. The Azapa Formation covers basement rocks on the
277 western side of the Western Andean Slope and has a thickness of 16 m, 41 m, and
278 260 m in holes 1, 2 and 7, respectively (Fig. 3). This is significantly thinner than
279 the ~500 m sequence exposed in the Central Basin (García *et al.*, 2004). These
280 lateral variations are compatible with the east-west transition from erosion of
281 the Western Cordillera to sedimentation in the Central Basin.

282

283 ***Oxaya Formation***

284 *The Poconchile ignimbrite and the overlying volcanoclastic member*

285 The Poconchile ignimbrite is less than 13 m thick and overlies the Azapa
286 Formation in holes 7 and 2, and can be traced along both the northern and
287 southern walls of the Lluta Quebrada. In the Molinos section, however, the
288 Quebrada is not deep enough to expose the Poconchile. The Poconchile is a
289 pinkish white to white in colour sillar-type ignimbrite. It contains white and
290 bright pink juvenile clasts between 1 mm and 10 cm in size. Lithic clasts are less
291 than 40 mm in size and mainly andesitic and granitic in composition. The
292 ignimbrite contains ~13% crystals, including plagioclase, quartz, sanidine,
293 biotite, and minor titanomagnetite, hornblende, zircon and apatite.

294 Clastic sedimentary deposits overlie the Poconchile ignimbrite in holes 7,
295 4, 2, 1, 3 and 10 with a thickness varying between 18 and 350 m. These deposits
296 contrast markedly with the Azapa Formation, in that the rocks are characterised
297 by couplets of matrix-poor graded breccia and coarse sandstone. Furthermore,
298 the clasts are mainly sub-angular rhyolites (ignimbrite) and andesites with sizes
299 varying from mm- to m-scale. The largest clasts are found in the easternmost
300 cores (3 and 10). In general, clasts become smaller and sandstone becomes more
301 abundant towards the west hole 4. The observation of breccia-sandstone
302 couplets as well as the sediment immaturity of the deposits suggests these rocks
303 were lahar deposits derived from an active volcanic terrain (Vallance, 2005).

304

305 *The Cardones ignimbrite*

306 The Cardones ignimbrite overlies the volcanoclastic member west of hole 1 and
307 basement lithologies east of hole 1. It has a thickness between 74 and 911 m
308 across the nine holes and its thickness generally thins towards the west and
309 south (Fig. 3). In the holes (7, 4, 2 and 9) located at the edges of the traverse, the
310 unit is covered by younger lithologies. In contrast, uplift and erosion exposed the
311 Cardones ignimbrite in the middle of the cross section.

312 The Cardones ignimbrite contains <5% juvenile clasts deformed into
313 fiamme that can be divided into 92-65% pinkish-white crystal-rich pumice clasts
314 (CRPs) (Fig. 4a and 4d) and 8-35% pale red crystal-poor pumice clasts (CPPs)
315 (Fig. 4b and 4e). Mingling of crystal-rich and crystal-poor juvenile material in a
316 single clast is observed (Fig. 4c). The ignimbrite also contains <1%
317 microcrystalline mafic enclaves that we call microdiorite clasts (Fig. 4f and 4h).

318 The bulk ignimbrite has a crystal content between 23.3 and 51.4%, with
319 an average of $42 \pm 17\%$ (2σ , $n=14$). The crystal assemblage contains quartz (3.6 -
320 18.2%), plagioclase (5.7 - 22%) and sanidine (1.6 - 15.5%), biotite (<4%),
321 titanomagnetite ($\leq 1\%$), hornblende ($\leq 1\%$), zircon, apatite and allanite. Almost
322 all crystals have been broken into fragments with sizes ranging from <0.5 to 5
323 mm (Fig. 4d). The majority of the original glass matrix is devitrified to
324 microcrystalline quartz and feldspar.

325 The crystal mode of CRPs varies between 31.7 and 56.2%, with an
326 average of $40 \pm 22\%$ (2σ , $n = 6$). The crystal assemblage contains quartz (6.1 -
327 20.7%), plagioclase (5.8 - 39.6%), sanidine (0 - 15.7%), biotite (<6%),
328 titanomagnetite ($\leq 1\%$), and accessory hornblende, zircon and apatite,
329 comparable to the bulk rock. Nevertheless, whereas sanidine is observed in all
330 bulk-rock samples, it may be absent in CRPs. Most crystals in CRPs are heavily
331 fractured, but the fragments are still closely held together and glass matrix often
332 fills the cracks in between the fractures (Fig 4d). In some CRPs, crystals lost their
333 initial shape and form bands of small (<1mm) crystal fragments (Fig. 4g).
334 Secondary alteration assemblages include calcite, barite, montmorillonite and
335 oxides formed after emplacement and are commonly observed in uncollapsed
336 pore spaces and in the crystal fractures.

337 CPPs have mineral assemblages that are similar to CRPs. Where CRPs
338 contain large euhedral crystals, CPPs only contain small sub-angular to rounded
339 crystal fragments surrounded by a red devitrified glass matrix (Fig. 4e). The
340 crystal fragments are on average smaller than 1 mm in size and the average
341 crystal mode for CPPs is $22.8 \pm 1.4\%$ (2σ , $n=3$).

342 Microdiorite clasts (Fig. 4f and 4h) predominantly consist of ~60%
343 microlites such as plagioclase, biotite, hornblende and minor magnetite in a
344 devitrified groundmass. Hornblende crystals are often heavily altered and are
345 found as crystal skeletons. Some crystals derived from the ignimbrite were
346 entrained in the microdiorites, a feature that indicates the microdiorites are
347 mafic enclaves.

348

349 *Subdivision of the Cardones ignimbrite*

350 General and detailed stratigraphic columns for the Cardones ignimbrite can be
351 found in Figures 3a and 5a, respectively. The vertical distribution of juvenile and
352 lithic clasts in each core is shown in Figures 5b and 5c. All fiamme aspect ratios
353 and densities are summarized in Figures 5d and 6, respectively.

354 Based on fiamme aspect ratios, densities, and observed stratigraphic
355 breaks, we distinguish two eruptive units within the Cardones ignimbrite.

356 *Unit 1.* The first (lower) unit is observed in all nine holes with a thickness
357 between 74 and 911 m. The welding intensity of unit 1 is inferred from vertical
358 profiles of fiamme aspect ratios and density measurements. In general, the
359 lowest average fiamme aspect ratios (~3) were measured at the top and base of
360 unit 1 and the highest values (up to ~9) in a few tens to hundreds of meters from
361 the base. Furthermore, bulk rock density is on average 2300 kg/m³ throughout
362 unit 1 and decreases to 1900 kg/m³ at the very top and base of the ignimbrite
363 (Fig. 6). Based on juvenile and lithic clast distributions (Fig. 5b and 5c) and
364 crystal modes (Supplementary material Table S3), four separate subunits can be
365 recognised within the first unit (Fig. 5 and 7). Subunit 1 and subunit 4 represent
366 the base and top of the first unit, respectively. The thickness of the subunits in

367 each core is presented in Table 1. Table 2 summarizes the characteristics of each
368 subunit, including colour, bulk crystallinity, bulk density, and details about
369 juvenile and lithic clasts. A more detailed description of each subunit can be
370 found in the supplementary material.

371 *Unit 2.* The second (upper) unit is only present in the two easternmost holes (6
372 and 9) with a thickness of 50 and 360 m. This unit is separated from the first unit
373 by a clear stratigraphic break, which is characterised by an interval of reworked
374 ignimbrite and sediments that is a few tens of centimeters thick. Furthermore,
375 unit 2 shows a separate welding profile with, on average, lower aspect ratios
376 than unit 1.

377

378 *The Molinos ignimbrite*

379 The Molinos ignimbrite is a pink to pinkish-white, weakly welded member. A
380 ~50 m thick interval of this ignimbrite is observed in the Molinos field section
381 (Fig. 2 and 3), where it is separated from the Cardones and Oxaya ignimbrites by
382 sedimentary intercalations of a few tens of metres thick. These sedimentary
383 intercalations pinch out towards the east and are not observed in the drill cores.
384 Drill hole and field observations indicate this ignimbrite is laterally
385 discontinuous, with only holes 7 and 4 containing a ~80 and ~40 m thick
386 interval of the Molinos ignimbrite.

387 The Molinos ignimbrite contains ~12% crystals of plagioclase, quartz,
388 sanidine, with minor biotite, amphibole, clinopyroxene, orthopyroxene,
389 titanomagnetite, zircon, monazite, and apatite. Pumice clasts are small and
390 dominantly rhyolitic, although small, more mafic, pumice clasts that mainly

391 contain pyroxene and hornblende are also observed. The Molinos ignimbrite
392 contains ~1% andesite lithic fragments smaller than 15 mm in size.

393

394 *The Oxaya ignimbrite*

395 The Oxaya ignimbrite is observed in the Molinos field section and holes 7, 4 and
396 2 (Fig. 3). Similar to García et al. (2004) we identify two eruptive units within the
397 Oxaya ignimbrite. The contact between the upper and lower unit is conformable.

398 *Lower unit:* The lower unit is unwelded to weakly welded and pink, light gray
399 and white in colour. The top of the lower unit is pink in colour. It contains ~15%
400 crystals, with quartz (6%), plagioclase (4%), sanidine (4%) and minor biotite,
401 titanomagnetite, amphibole, zircon and apatite. This unit contains ~1% andesite
402 lithic fragments smaller than 30 mm in size. The lower unit is observed in the
403 Molinos field section, hole 7, 4 and 2 with a thickness between ~10 and ~70 m.

404 *Upper unit:* The upper unit is a reddish gray to pinkish white, moderately to
405 intensely welded ignimbrite with a clear eutaxitic texture. The majority of the
406 upper unit contains ~34% crystals, including quartz (6 – 11%), plagioclase (7 –
407 14%), sanidine (10 –12%), biotite (~1%), and minor titanomagnetite,
408 hornblende, zircon, apatite and monazite. Towards the base the crystallinity
409 decreases to ~25%. The upper unit contains <<1% lithic clasts. This unit is
410 observed in the Molinos field section, hole 7 and hole 4 with a thickness between
411 ~90 m and ~20 m. North of the Lluta Quebrada the Oxaya ignimbrite
412 experienced significant erosion and thus the drill cores contain limited material
413 of this ignimbrite. However, south of the Lluta Quebrada the Oxaya ignimbrite is
414 well preserved and the upper unit has a thickness up to a few hundreds of
415 metres thick (e.g. Garcia et al. 2004).

416

417 **U-Pb geochronology of the Oxaya Formation**

418 The U-Pb isotope data for 39 zircons are presented in Figure 8. The complete
419 data table, can be found in the supplementary material. The $^{206}\text{Pb}/^{238}\text{U}$ dates of
420 the individual samples scatter over 0.1 to 1 Myr, more than the analytical
421 uncertainty. Explanations of this data spread include magmatic processes, such
422 as protracted crystal growth prior to eruption, the inheritance of xenocrysts and
423 antecrysts, and post-depositional Pb-loss (Sahy et al., 2015). Nevertheless, Sahy
424 et al. (2015) showed that it is statistically valid to represent the eruption age of a
425 volcanic rock by calculating the weighted mean age of the youngest coherent
426 zircon population. Each youngest population must contain three or more
427 $^{206}\text{Pb}/^{238}\text{U}$ dates and give an MSWD that is acceptable for a single population
428 (Wendt and Carl, 1991).

429 The youngest zircon population for the Poconchile ignimbrite (sample
430 133017) gives a weighted mean age of $22.736 \pm 0.021/0.021/0.032$ Ma ($n = 3$,
431 MSWD = 1.7), which is within uncertainty of the previously obtained $^{40}\text{Ar}/^{39}\text{Ar}$
432 sanidine age of 22.72 ± 0.15 Ma (Wörner *et al.*, 2000).

433 The weighted mean age of the youngest zircon populations of the three
434 samples derived from the Cardones ignimbrite unit 1 are: a) $21.909 \pm$
435 $0.036/0.037/0.043$ ($n = 3$, MSWD = 0.79), sample 130061 (base subunit 1); b)
436 $21.947 \pm 0.017/0.018/0.029$ Ma ($n = 4$, MSWD = 1.6), sample 901 (base subunit
437 2); c) $21.914 \pm 0.015/0.017/0.029$ Ma ($n = 5$, MSWD = 0.57), sample 130008p
438 (subunit 3). The three weighted means overlap within uncertainty. In order to
439 find a representative eruption age for unit 1, the $^{206}\text{Pb}/^{238}\text{U}$ dates of the three
440 samples were combined. The weighted mean age of the youngest coherent

441 population is 21.924 ± 0.011 Ma ($n=10$, MSWD = 1.14). From core observations
442 we observe that a short break in the eruption occurred between unit 1 and 2.
443 This break was long enough to rework some of the ignimbrite at the top of unit 1
444 and deposit thin sedimentary layers prior to the deposition of unit 2. The
445 youngest zircon population for unit 2 (sample 913) gives a weighted mean date
446 of $21.946 \pm 0.012/0.013/0.027$ Ma ($n = 4$, MSWD = 1.42), which is within
447 uncertainty with the weighted mean age of unit 1. Therefore, we were unable to
448 resolve the length of this time gap with high-precision U-Pb isotope dating.

449 The youngest coherent zircon populations of samples 130032 and F16,
450 collected from the lower and upper units of the Oxaya ignimbrite respectively,
451 give a weighted mean age of $19.711 \pm 0.036/0.036/0.052$ Ma ($n = 4$, MSWD =
452 1.4) and $19.698 \pm 0.064/0.065/0.068$ Ma ($n = 5$, MSWD = 1.7). Both weighted
453 mean ages are within uncertainty at the 2σ confidence level. These ages are also
454 within uncertainty with the $^{40}\text{Ar}/^{39}\text{Ar}$ sanidine age determined for the Oxaya
455 ignimbrite by García et al. (2004) and Wörner et al. (2000).

456

457 **Chemical composition of the Oxaya Formation**

458 ***The Cardones ignimbrite***

459 Representative analyses of major and trace element concentrations are
460 presented in Table 3 and the full data set can be found in the supplementary
461 material. Overall the CRPs and CPPs are rhyolites with normalized SiO_2 content
462 of between 69.6 -77.5 wt% and 72.2-76.0 wt%, respectively (Fig. 9a, 9b). K_2O
463 first increases with SiO_2 and then decreases at a SiO_2 composition of ~ 75 wt%
464 (Fig. 9b). CRPs have large variations in Ba and Eu/Eu^* that ranges between 450-
465 1150 ppm and 1-0.45, respectively. In contrast, Dy/Yb values are constant (Fig.

466 9d). La/Yb values vary between 10 and 30 and Rb/Sr values between 0.3 and 1.2.
467 Chondrite normalized REE patterns indicate enrichment of LREE, a negative Eu-
468 anomaly and a MREE minima (Fig. 9f).

469 Compared to juvenile clasts, the bulk rock analyses show a more
470 restricted compositional range, with normalized SiO₂ values between 72.0 and
471 77.5 wt%, Ba values between 650 and 850 ppm and Eu/Eu* values between >0.6
472 and <0.8. The average major and trace element compositions are plotted for both
473 the CRPs and the bulk rock (excluding samples with LOI larger than 5) (Fig. 9a -
474 e). Compared to CRPs, Bulk rock samples are enriched in compatible elements
475 such as Na₂O, Eu, and Ba, and depleted in incompatible elements such as HREE.
476 The average SiO₂ concentration in the bulk rock is similar to the average
477 concentration in CRPs.

478 Fig. 9g shows the geochemistry of bulk rock and CRPs plotted against the
479 depth in hole 1. The absence of CRP data at the base of the ignimbrite is because
480 of the lack of sample-sized unaltered pumice. The CRPs show significant
481 variations in Ba and Zr/Nb values, but not in any systematic trend. In
482 comparison, the bulk rock samples are more homogeneous throughout the
483 ignimbrite. The depletion of SiO₂ and Ba in the bulk rock at the base of subunit 1
484 is attributed to alteration; clay minerals are observed in thin section and this
485 interpretation is supported by the LOI-values ≥5wt%. Furthermore, throughout
486 the ignimbrite Ba and Zr/Nb values are related, but at the base the fluid-mobile
487 element Ba is depleted whereas the fluid-immobile trace-element ratio Zr/Nb is
488 not changed.

489 The microdiorites (mafic enclaves) are less evolved and have a
490 normalized SiO₂ content between 59.4 - 63.5 wt% and can be classified as

491 andesite-dacite (Fig 9a). In general the microdiorites have lower Ba (<700 ppm)
492 and La/Yb (<15) concentrations, similar Eu/Eu* and Dy/Yb values to CRPs. The
493 REE patterns also indicate a negative Eu-anomaly and a MREE-minimum.

494

495 ***The Molinos and Oxaya ignimbrites***

496 Major and trace element compositions of the Molinos ignimbrite are similar to
497 the Cardones ignimbrite, although Ba concentrations are slightly higher (Fig. 9c
498 and 9d). Figure 9h shows that also the Molinos ignimbrite doesn't show any
499 evidence for vertical zonation.

500 The Oxaya ignimbrite has a high average normalized SiO₂ and K₂O
501 content of ~77 wt% and ~4.5 wt% respectively (Fig 9a and 9b). The lower unit
502 as well as the base of the upper unit are depleted in Ba, Eu/Eu* and La/Yb and
503 enriched in Rb/Sr compared to the top of the upper unit (Fig. 9c-9f). In general
504 the lower unit and the base of the upper unit contain Ba ~300 ppm, Rb/Sr ~5
505 and La/Yb ~ 10, whereas the top of the upper subunit contains Ba ~900 ppm,
506 Rb/Sr ~1 and La/Yb ~25 (Fig. 9). The correlation between Ba and Zr/Nb
507 suggests this is a magmatic rather than an alteration trend (Fig. 9h).

508

509 **Discussion**

510 ***Geochemical signatures***

511 The ignimbrites in the Oxaya Formation are high-SiO₂ rhyolites with plagioclase,
512 quartz, sanidine, biotite and titanomagnetite as the major crystal phases. The
513 MREE minimum (Fig. 9f) indicates amphibole control on the magma evolution.
514 However, the constant MREE/HREE values (Fig. 9d) together with the limited
515 amounts of amphibole in the ignimbrites suggest that amphibole mainly

516 fractionated from deeper precursory, more mafic magmas or that there was
517 residual amphibole in the source region during crustal partial melting. The trace
518 element geochemistry indicates that plagioclase and sanidine mainly controlled
519 the magmatic signatures. For example the sanidine-poor CRPs in the Cardones
520 ignimbrite have high Ba (>800 ppm) and high Eu/Eu* (>0.7) values and a
521 positive correlation between K₂O and SiO₂, values that indicate limited fractional
522 crystallization of plagioclase and no crystallization of sanidine. In contrast, the
523 sanidine-rich CRPs have low Ba (<550 ppm) and low Eu/Eu* (<0.5) values, and
524 an inverse correlation between K₂O and SiO₂. These observations imply
525 significant fractional crystallization of both sanidine and plagioclase. Also the
526 strong variations in Ba, Eu/Eu* and Rb/Sr between the lower unit and upper unit
527 in the Oxaya ignimbrite suggests strong control of sanidine and plagioclase.

528

529 ***Magma crystallinity, zoning and heterogeneity***

530 Our observations place some constraint on the internal organisation of the
531 magma reservoirs that sourced the ignimbrites and the processes prior to and
532 during eruption. We have documented marked variations in crystallinity of the
533 Oxaya Formation ignimbrites, both within a single ignimbrite and between the
534 different ignimbrites. Bachmann and Bergantz (2004) suggested that high-SiO₂
535 crystal-poor rhyolites, such as the Molinos ignimbrite and the lower unit of the
536 Oxaya ignimbrite represent melt-rich magmas extracted from locked crystal
537 mushes, where crystallinity is $\geq 50\%$. The highly evolved crystal-poor lower unit
538 of the Oxaya ignimbrite and the overlying less-evolved more crystal-rich upper
539 unit (Fig. 9h) conforms to the classic zoning of many ignimbrites (Smith 1979,
540 Hildreth 1981; Hildreth and Wilson, 2007).

541 A common model applied to the generation of crystal-rich ignimbrites
542 such as the Cardones is reheating and convective stirring of locked (>50%
543 crystals) crystal mushes driven by heat and volatiles derived from underplating
544 more mafic magmas (Bachmann and Bergantz, 2006, Huber *et al.*, 2012,
545 Parmigiani *et al.*, 2014,). In the case of the Fish Canyon Tuff, the defrosting model
546 is consistent with the presence of abundant resorbed crystals, mafic enclaves
547 that have been linked to the underplating magmas (Bachmann *et al.*, 2002), and
548 systematic changes in zircon trace element chemistry with time (Wotzlaw *et al.*,
549 2013). Some features of the Cardones ignimbrite are consistent with the
550 unlocking concept: (1) homogeneous bulk composition (Fig. 9); (2) mafic
551 enclaves (microdiorites); and (3) non-systematic vertical variation in pumice
552 geochemistry (Fig. 9g). However, the crystal content of the ignimbrite is mostly
553 lower (~40%) than expected if the magma body started off as a locked crystal
554 mush (>50%). Furthermore, the absence of resorbed crystals as expected for a
555 reheating event discounts crystal dissolution as a mechanism to account for
556 crystal contents, which, although high, are well below the unlocking threshold. In
557 addition, the reheating model predicts a homogenous composition of both bulk
558 rock and pumice (e.g. Huber *et al.*, 2012). However, juvenile clasts from the
559 Cardones ignimbrite contain significant variations in crystal content (32 to
560 56%), crystal proportions (sandine-rich and sandine-free pumice) and trace
561 element composition. The magmatic system thus had significant local
562 heterogeneities. The even distribution of these heterogeneities throughout the
563 ignimbrite (e.g. Fig. 9g) indicates processes of homogenization of a
564 heterogeneous magma system prior to and perhaps during eruption. Alternative

565 processes to defrosting are implied by the observations in the Cardones
566 ignimbrite.

567 Evidence for compositional heterogeneity is also observed in other cases
568 where juvenile clasts from large-volume ignimbrites have been studied (Lindsay
569 *et al.*, 2001, Maughan *et al.*, 2002, Wilson and Hildreth *et al.*, 2007, Wright *et al.*,
570 2011). There is additional evidence for chemical and isotopic heterogeneities in
571 crystals (e.g. Hildreth *et al.* 1981; Cooper *et al.*, 2012; Ellis *et al.*, 2014, Wotzlaw
572 *et al.*, 2015). Cashman and Giardano (2014) suggested that heterogeneities in
573 both crystal-rich and crystal-poor ignimbrites can be explained by a complex
574 lens-dominated magma reservoir in which each magma lens has a distinct trace
575 element and isotopic composition. During a single eruption, multiple magma
576 lenses can be amalgamated and erupt together, giving rise to the observed
577 heterogeneities. The heterogeneities distributed throughout the Cardones
578 supports the idea of destabilization of a complex lens-dominated magma
579 reservoir with mixing of different magmas. The process of destabilization and
580 reorganisation of the magma system with implied mixing of different magma
581 bodies might have caused the eruption. The bulk rock in the Cardones ignimbrite
582 lacks the heterogeneities observed in the juvenile casts and thus intense physical
583 homogenization is inferred during the eruption.

584

585 ***Controls on lithic and juvenile clast content in the Cardones ignimbrite***

586 The lithic and juvenile clasts content of an ignimbrite can give valuable
587 information about the eruption dynamics and the distance to the source caldera
588 (e.g. Wilson and Hildreth, 1997). Absence of proximal lithofacies in the Cardones

589 ignimbrite, such as volcanic lag breccias, leads us to infer medial and distal
590 outflow settings.

591 The crystal-rich pumice (CRP) and crystal-poor pumice (CPP) clasts in the
592 Cardones ignimbrite have similar chemical compositions but distinct textures
593 (Fig. 4 and 9). This observation suggests that physical rather than chemical
594 processes caused the difference. Two types of pumice with characteristic similar
595 to those described for the Cardones ignimbrite have been found in the
596 pyroclastic products from the climactic eruption of Mount Pinatubo in the
597 Philippines on 15 June 1991 (Polacci *et al.*, 2001), and the 800 yr B.P. Plinian
598 eruption of the Quilotoa Volcano in Ecuador (Rosi *et al.*, 2004). These authors
599 suggested that shearing of phenocryst-rich magma along the conduit wall could
600 cause heating of the magma and brecciation of crystals resulting in texturally
601 different, but chemically similar pumice. The lower crystal content of the crystal-
602 poor pumice is attributed to crystal grinding and resorption (Rosi *et al.*, 2001).
603 We suggest that a comparable process formed the CPPs in the Cardones
604 ignimbrite. We furthermore suggest that the CRPs with extremely fractionated
605 crystals (Fig. 4g) also suffered cataclastic flow along the conduit like the CPPs.

606 The proportion of CPPs relative to CRPs in the Cardones ignimbrite
607 decreases gradually from the base to the top; in subunit 1, 2, 3 and 4, CPPs
608 account for 50%, 33%, 15% and <1% of the total juvenile clasts content,
609 respectively. This observation could imply that the start of the eruption involved
610 either more intense shearing along the caldera walls or narrower conduits, or
611 both. Thus the decline in the proportion of CPP upwards in the stratigraphy
612 might reflect widening of conduit systems. Subsidence along outward dipping
613 ring fractures provides such a mechanism (Druitt and Sparks 1984).

614 Furthermore, the general decline of granitic and andesitic lithic clasts upwards in
615 unit 1 suggests more conduit wall erosion took place during the first part of the
616 eruption. Abundant silicic ignimbrite clasts in subunit 4 are typically similar
617 (crystal content, textures and colour) to the Cardones ignimbrite itself, and could
618 therefore be recycled from earlier erupted intra- and extra-caldera material (e.g.
619 subunit 1-3).

620

621 ***Thickness of the Cardones ignimbrite and pre-eruptive topography***

622 Across the Central Basin and Precordillera around the Lluta Quebrada the extra-
623 caldera, post-welding thickness of medial and distal deposits of the Cardones
624 ignimbrite ranges from 300 to 900 m, with an average thickness of ~550 m. In
625 fact, the 900 m thick sequence of the ignimbrite in hole 1 is not the full thickness.
626 Due to erosion subunit 4 and parts of subunit 3 are not preserved in the holes
627 located near the hinge of the Huaylillas anticline (Fig. 5a). Subunit 4 is at least
628 110 m thick in drill holes where the Cardones ignimbrite is well preserved
629 (Table 1). We therefore infer that the full thickness of the Cardones ignimbrite in
630 drill hole 1 exceeded 1000 m. Large-volume ignimbrites with a thickness ≥ 1000
631 m are commonly linked to intra-caldera fills (e.g. Willcock et al. 2013). However,
632 even where the Cardones has a post-welding thickness of ~1000 m, evidence
633 points to outflow deposits. The great variation in thickness of the Cardones
634 ignimbrite across the Precordillera (Table 1) implies that the outflow sheet was
635 emplaced over a highly irregular topography with deep valleys that were
636 completely in-filled by the ignimbrite. We suggest that significant topographic
637 relief in the Precordillera already existed prior to 21.9 Ma, and thus that
638 exhumation and rock uplift rates were high at this time (e.g. Montgomery and

639 Brandon, 2002). This conclusion is consistent with the observed lateral
640 variations in the Azapa Formation that suggest east-west transition from erosion
641 of the Western Cordillera and the east part of the Precordillera to sedimentation
642 in the Central Basin. The great thickness of the Cardones outflow sheet can be
643 attributed to filling of a deep palaeo-valley comparable to the present-day Lluta
644 quebrada, which is up to 1.7 km deep.

645

646 ***Welding of the Cardones ignimbrite***

647 Flattening of juvenile clasts is related to the intensity of welding (Peterson, 1979,
648 Quane and Russell, 2005). Therefore, the aspect ratios of juvenile clasts (fiamme)
649 (Fig 5d) are used to: (1) quantify the welding processes and (2) calculate the pre-
650 welding thickness of the Cardones ignimbrite. Here we assume that the fiamme
651 are formed post-depositionally, through compaction and welding controlled by
652 residence time above the glass transition temperature, dissolution and
653 compression of volatiles, and the overlying load of the ignimbrite (Riehle *et al.*,
654 1995, Sparks *et al.*, 1999, Russell and Quane, 2005, Quane and Russell, 2005).
655 Nevertheless, pumice fiamme deformation can occur to increase aspect ratios
656 during syn-depositional processes via agglutination of hot glass and pumiceous
657 material (e.g. Branney and Kokelaar, 1992; Smith and Cole, 1997; Kobberger and
658 Schmincke, 1999). Therefore, the calculated values in the following paragraphs
659 will be maximum numbers.

660

661 ***Aspect ratios and density***

662 The fiamme aspect ratio profiles (Fig. 5d) show variation between the two
663 pumice types as well as across the different drill holes. The vertical aspect ratio

664 profiles for CRPs and CPPs show similar trends, but CPPs have on average ~30%
665 higher aspect ratios than CRPs. More initial pore space and the absence of large
666 obstructive crystals may explain the extra flattening of the CPPs. In the following
667 section we will work from the CRP aspect ratio profiles as these are based on
668 significantly more data.

669 In holes 9 and 3, where subunit 1 and 2 are either thin or absent, the
670 mean aspect ratios of CRPs rapidly increases in the basal ~50 m of the
671 ignimbrite, from values of ~3.0 to values larger than 8.0. Moving upwards, the
672 aspect ratios gradually decrease to values ~2.7 at the top of subunit 4. This trend
673 can be explained by the increase in overburden with depth and that the top and
674 base of the ignimbrite would have cooled faster than the centre. The
675 asymmetrical profile may also indicate more efficient cooling at the surface
676 compared to heat loss at the base of the ignimbrite (see models by Riehle et al.
677 1995). However, in holes where the lithic-rich subunits 1 and 2 are present (Fig
678 5d, drill holes 7, 1, 5), the mean aspect ratio is relatively low with a mean value of
679 ~4.0. At the base of the lithic-poor subunit 3, the aspect ratio markedly increases
680 towards values of ~7.0. From there, the values gradually decrease towards ~2.7
681 at the top of subunit 4. The anomalously low aspect ratios in subunit 2 might be
682 caused by the entrainment of cold lithic clasts (subunit 2 contains on average 4%
683 lithic clasts that are <60 mm in size – Table 2). Marti et al. (1991) showed that
684 entrainment of cold lithics between 10 and 100 mm in size will thermally
685 equilibrate with the ignimbrite within seconds to tens of minutes. Therefore the
686 chilling due to cold lithics in subunit 2 could have led to the glass viscosity of
687 juvenile clasts being increased during welding. Cooling by 4% lithics is estimated
688 at approximately 30°C for a melt at 750°C, which results in almost an order of

689 magnitude increase in glass viscosity (Giordano et al., 2008) and complementary
690 order of magnitude decrease in compaction rate, The pumice fiamme in subunit
691 2 are consequently less flattened compared to lithic-free parts of the ignimbrite.

692 The density data for hole 1 show that the top and base of the ignimbrite
693 had a density of $\sim 1900 \text{ kg/m}^3$ compared to $\sim 2300 \text{ kg/m}^3$ for the rest of unit 1
694 (Fig. 6). Working from the assumption that bulk rock with a density of 1900
695 kg/m^3 preserved all its pore space and bulk rock with a density of 2300 kg/m^3
696 lost all its pore space, we calculate that the bulk rock porosity was $\sim 20\%$. Since
697 the bulk rock has $\sim 40\%$ crystals with zero porosity, the porosity of the glassy
698 matrix must have been $\sim 30\%$. Previous studies have demonstrated a close
699 relationship between flattening of juvenile clasts and the density of the matrix
700 (e.g. Quane and Russell, 2005). However, the density profile for the bulk matrix
701 in hole 1 is apparently decoupled from the flattening of juvenile clasts, as it does
702 not show a decrease in density with the increased lithic content in subunit 2 (Fig.
703 6). This might imply that the welding and compaction of the $\sim 30\%$ matrix glass
704 porosity occurred before the cold lithic clasts could have had any significant
705 effect on the glass viscosity of matrix glass. This suggests that welding and
706 compaction of the bulk rock must have occurred almost instantly after eruption,
707 whereas flattening of juvenile clasts occurs over longer time scales.
708 Consequently, welding of the bulk rock via syn-depositional agglutination likely
709 played a role in the Cardones ignimbrite.

710

711 *Thickness reduction during welding and compaction processes*

712 Taking into account the variable densities for the different subunits in the
713 Cardones ignimbrite, the reduction of $\sim 30\%$ matrix glass pore-space results in

714 an almost instantaneous thickness reduction of about ~16%. Based on pore
715 space elimination in juvenile clasts we can also calculate the thickness reduction
716 due to the flattening of fiamme during post-depositional welding. Investigating
717 the original percentage of pore space in the pumice is complicated due to
718 welding, devitrification and the growth of secondary minerals in initial pore
719 spaces. However, we make a rough estimation of the initial pore space by
720 assuming that welding was fully accommodated by porosity reduction in initially
721 spherical pumices with a unit aspect ratio. Thus flattened pumice clasts are
722 ellipsoids defined by two one-unit radii (in the horizontal plane) and one radius
723 that is the inverse of the measured aspect ratio (in the vertical plane). By
724 subtracting the volume of the ellipsoid (deflated pumice) from the volume of the
725 unit sphere (inflated pumice), the percentile volume loss can be calculated.

726 For example, if we assume that CRPs and CPPs in the most welded subunit
727 3 lost all their initial pore space (which is supported by observations in thin
728 section Fig. 4a, 4d, 4g), the average aspect ratios of CRP (5.4) and CPP (7.2) for
729 subunit 3 give an average porosity of ~80% and 85%, respectively. However, it
730 is important to bear in mind that the high variation in aspect ratios measured on
731 CRPs and CPPs as well as the variation in CRP density (Fig. 5), likely reflects large
732 variations in the initial porosity, shape, and orientation of the pumices prior to
733 flattening.

734 Using the assumptions described above the maximum post-depositional
735 unwelded thickness (X_0) is calculated for each subunit with equation (1):

736

$$737 X_0 = (X_{CRP} \times AR_{CRP} + X_{CPP} \times AR_{CPP}) * IP_{juv} / 100 * X_w \quad (1)$$

738

739 where X_{CRP} and X_{CPP} are the relative fractions of CRP and CPP. AR_{CRP} and AR_{CPP}
740 are the average aspect ratios for CRP and CPP (Table 2). IP_{juv} is the intersection
741 percentage for juvenile clasts and X_w is the observed welded thickness of the
742 Cardones of each subunit (Table 1). We find that by eliminating pore space in the
743 juvenile clasts, the thickness of the ignimbrite is reduced by ~14%. This
744 calculation estimates that the maximal post-depositional unwelded thickness of
745 the Cardones ignimbrites was ~1100 m.

746

747 **Conclusions**

748 Our combined stratigraphic, volcanological, geochronological, and geochemical
749 study of the large volume ignimbrites from the early Miocene Oxaya Formation
750 provides fundamental insights into the pre-, syn- and post-eruptive processes
751 related to these rare, but extensive ignimbrites.

752 (1) In northernmost Chile at ~18° the early Miocene ignimbrite flare-up is
753 characterised by the Oxaya Formation. At the base of the formation is the 22.736
754 ± 0.021 Ma Poconchile ignimbrite, which is covered by a series of volcanoclastic
755 rocks that include lahar deposits. Subsequently, at 21.924 ± 0.011 Ma at least
756 1260 km^3 (García et al., 2004) of pyroclastic material, currently known as the
757 Cardones ignimbrite, erupted. The Cardones ignimbrite was followed by the
758 deposition of the Molinos ignimbrite and finally the 19.711 ± 0.036 Ma Oxaya
759 ignimbrite.

760 (2) The ignimbrites of the Oxaya Formation ignimbrite are high-SiO₂ rhyolites
761 with a wide range of crystallinities (~10 – 50%). The ignimbrites are derived
762 from magmatic systems that contain significant heterogeneities in crystal
763 content, mineral proportions and trace-element compositions. The Oxaya

764 ignimbrite is zoned and can be linked to the incremental extraction of a
765 relatively crystal-poor magma overlying a less-evolved crystal-rich magma. In
766 contrast, marked heterogeneities in pumice types, crystal content and pumice
767 mineral assemblages are distributed throughout the Cardones ignimbrite. We
768 infer magma mixing linked to destabilization of a complex lens-dominated
769 magmatic system.

770 (3) During eruption the eruption of the Cardones ignimbrite, intense physical
771 magma homogenization of the bulk rock took place. The origin of both crystal-
772 rich and crystal-poor pumice types in the Cardones ignimbrite is attributed to
773 shearing of crystal-rich magma in the conduit along ring fractures. Changes in
774 the relative abundance of crystal-poor pumice, lithic content and lithic
775 lithologies indicates conduit widening throughout the eruption.

776 (4) Medial and distal outflow sheets of the Cardones ignimbrite covered the
777 entire Precordillera in northernmost Chile. The welded thickness of the
778 ignimbrite varies between ~500 and 1000 m in the Precordillera, suggesting the
779 ignimbrite covered an area with a significant topography and accumulated in
780 deep valleys.

781 (5) Both compaction and welding resulted in a maximum thickness reduction of
782 around 30% for the Cardones ignimbrite. A decrease in the aspect ratio of
783 pumice fiamme with increased lithic content is explained by the cooling effects in
784 lithics which increases the glass viscosity and decreases pumice deformation
785 rates

786

787 **Acknowledgments**

788 This project was funded by BHP Billiton and we thank them for supporting this
789 research. Special thanks to Christopher Ford and all the other staff based in Chile
790 that assisted us in the field and core-shed. Funding for U-Pb zircon analyses was
791 provided by Natural Environment Research Council NIGFC grant IP-1466-1114.
792 Analytical work would not have been possible without technical support from
793 Simon Tapster and Nicola Atkinson. We also thank Iain McDonald for his
794 assistance with the ICP-MS and ICP-OES analyses at Cardiff University. The
795 manuscript has benefited greatly from reviews by J-F Wötzel and an
796 anonymous reviewer. We also like to thank Moyra Gardeweg for her feedback on
797 this work. The extensive data set from the drill holes was acquired with the
798 invaluable help of Courtney Jiskoot, Amy Gilmer, and Brad West.

799

800 **References**

- 801 Allmendinger, R.W., Jordan, T.E., Kay, S.M. & Isacks, B.L., 1997. The evolution of
802 the Altiplano-Puna plateau of the Central Andes, *Annual review of earth
803 and planetary sciences*, **25**,
804 <http://dx.doi.org/10.1146/annurev.earth.25.1.139>
- 805 Bachmann, O., & Bergantz, G. W., 2004, On the origin of crystal-poor rhyolites:
806 extracted from batholithic crystal mushes, *Journal of Petrology*, **45**, 1565-
807 1582, <http://dx.doi.org/10.1093/petrology/egh019>
- 808 Bachmann, O. & Bergantz, G.W., 2006. Gas percolation in upper-crustal silicic
809 crystal mushes as a mechanism for upward heat advection and
810 rejuvenation of near-solidus magma bodies, *Journal of Volcanology and
811 Geothermal Research*, **149**, 85-102,
812 <http://dx.doi.org/10.1016/j.jvolgeores.2005.06.002>
- 813 Bachmann, O., Bergantz, G., 2008, The magma reservoirs that feed
814 supereruptions. *Elements*, **4**, 17-21,
815 <http://dx.doi.org/10.2113/GSELEMENTS.4.1.17>
- 816 Bachmann, O., Dungan, M.A. & Lipman, P.W., 2002. The Fish Canyon magma body,
817 San Juan volcanic field, Colorado: rejuvenation and eruption of an upper-
818 crustal batholith, *Journal of Petrology*, **43**, 1469-1503.
819 <http://dx.doi.org/10.1093/petrology/43.8.1469>
- 820 Best, M.G. & Christiansen, E.H., 1997. Origin of broken phenocrysts in ash-flow
821 tuffs, *Geological Society of America Bulletin*, **109**, 63-73,
- 822 Blanco, N., Vásquez, P., Sepúlveda, F., Tomlinson, A. J., Quezada, A., Ladino, M.,
823 2012, Levantamiento geológico para el fomento de la exploración de

824 recursos minerales e hídricos de la Cordillera de la Costa, Depresión
825 Central y Precordillera de la Región de Tarapacá (20-21 S). *Servicio*
826 *Nacional de Geología y Minería*, Informe Registrado IR-12-50, 7
827 Branney, M. J., Kokelaar, P., 1992, A reappraisal of ignimbrite emplacement:
828 progressive aggradation and changes from particulate to non-particulate
829 flow during emplacement of high-grade ignimbrite. *Bulletin of*
830 *Volcanology*, **54**, 504-520.
831 Bowring, J., McLean, N. & Bowring, S., 2011. Engineering cyber infrastructure for
832 U - Pb geochronology: Tripoli and U - Pb_Redux, *Geochemistry,*
833 *Geophysics, Geosystems*, **12**, <http://dx.doi.org/10.1029/2010GC003479>
834 Cashman, K.V. & Giordano, G., 2014. Calderas and magma reservoirs, *Journal of*
835 *Volcanology and Geothermal Research*, **288**, 28-45,
836 <http://dx.doi.org/10.1016/j.jvolgeores.2014.09.007>
837 Charrier, R., Hérail, G., Pinto, L., García, M., Riquelme, R., Farías, M. & Muñoz, N.,
838 2013. Cenozoic tectonic evolution in the Central Andes in northern Chile
839 and west central Bolivia: implications for paleogeographic, magmatic and
840 mountain building evolution, *International Journal of Earth Sciences*, **102**,
841 235-264, <http://dx.doi.org/10.1007/s00531-012-0801-4>
842 Chesner, C.A., 1998. Petrogenesis of the toba tuffs, Sumatra, Indonesia, *Journal of*
843 *Petrology*, **39**, 397-438.
844 Chesner, C.A. & Rose, W.I., 1991. Stratigraphy of the Toba tuffs and the evolution
845 of the Toba caldera complex, Sumatra, Indonesia, *Bulletin of Volcanology*,
846 **53**, 343-356.
847 Christensen, M., Pérez, G., Montecinos, F. & Curtis, G., 1969. Late Cenozoic
848 volcanism, deformation and denudation in northern Chile. in *Berkeley-*
849 *Inst. Invest. Geol. Chile* Dept. Geol. Geophys., Univ. of California.
850 Christiansen, R. L, 2001, The Quaternary and pliocene Yellowstone plateau
851 volcanic field of Wyoming, Idaho, and Montana (No. 729-G).
852 Condon, D., Schoene, B., McLean, N., Bowring, S. & Parrish, R., 2015. Metrology
853 and Traceability of U-Pb Isotope Dilution Geochronology (EARTHTIME
854 Tracer Calibration Part I), *Geochimica et Cosmochimica Acta*, **164**, 464-
855 480, <http://dx.doi.org/10.1016/j.gca.2015.05.026>
856 Cooper, G. F., Wilson, C. J., Millet, M. A., Baker, J. A., Smith, E. G., 2012, Systematic
857 tapping of independent magma chambers during the 1Ma Kidnappers
858 supereruption, *Earth and Planetary Science Letters*, **313**, 23-33,
859 <http://dx.doi.org/10.1016/j.epsl.2011.11.006>
860 De Silva, S., 1989. Altiplano-Puna volcanic complex of the central Andes, *Geology*,
861 **17**, 1102-1106.
862 De Silva, S., Zandt, G., Trumbull, R., Viramonte, J.G., Salas, G. & Jiménez, N., 2006.
863 Large ignimbrite eruptions and volcano-tectonic depressions in the
864 Central Andes: a thermomechanical perspective, *Geological Society,*
865 *London, Special Publications*, **269**, 47-63.
866 Druitt, T.H., Sparks, R.S.J., 1984, On the formation of calderas during ignimbrite
867 eruptions, *Nature*, **310**, 679-681.
868
869 Ellis, B. S., Bachmann, O., Wolff, J. A., 2014, Cumulate fragments in silicic
870 ignimbrites: The case of the Snake River Plain, *Geology*, **42**, 431-434.
871 <http://dx.doi.org/10.1130/G35399.1>

- 872 Farías, M., Charrier, R., Comte, D., Martinod, J. & Hérail, G., 2005. Late Cenozoic
873 deformation and uplift of the western flank of the Altiplano: Evidence
874 from the depositional, tectonic, and geomorphologic evolution and
875 shallow seismic activity (northern Chile at 19°30'S), *Tectonics*, **24**,
876 <http://dx.doi.org/10.1029/2004TC001667>
- 877 Francis, P.W., Sparks, R., Hawkesworth, C., Thorpe, R., Pyle, D., Tait, S., Mantovani,
878 M. & McDermott, F., 1989. Petrology and geochemistry of volcanic rocks
879 of the Cerro Galan caldera, northwest Argentina, *Geological Magazine*,
880 126, 515-547.
- 881 Garcia, M., Gardeweg, M., Hérail, G. & Pérez de Arce, C., 2000, IX Congreso
882 Geológico Chileno, **2**, 286-290.
- 883 Garcia, M. & Hérail, G., 2005. Fault-related folding, drainage network evolution
884 and valley incision during the Neogene in the Andean Precordillera of
885 Northern Chile, *Geomorphology*, **65**, 279-300,
886 <http://dx.doi.org/10.1016/j.geomorph.2004.09.007>
- 887 García, M., Gardeweg, M., Clavero, J. & Hérail, G., 2004. Arica map: Tarapacá
888 Region, scale 1: 250,000, *Serv. Nac. Geol. Min*, **84**, 150.
- 889 García, M., Hérail, G. & Charrier, R., 1996. The cenozoic forearc evolution in
890 northern Chile: The western border of the Altiplano of Belén (Chile). *in*
891 *the Third International Symposium of Andean Geodynamics*, pp. 359-362.
- 892 García, M., Riquelme, R., Farías, M., Hérail, G. & Charrier, R., 2011. Late Miocene–
893 Holocene canyon incision in the western Altiplano, northern Chile:
894 tectonic or climatic forcing?, *Journal of the Geological Society*, 168, 1047-
895 1060.
- 896 Gardeweg, M. & Sellés, D., 2013. Geología del área Collacagua-Rinconada, Región
897 de Tarapacá. *in Carta Geológica de Chile, Serie Geología Básica* **148**, p122,
898 *mapa escala 1:100.000*, ed Minería, S. N. d. G. y., Santiago.
- 899 Geyer, A. & Marti, J., 2008. The new worldwide collapse caldera database (CCDB):
900 A tool for studying and understanding caldera processes, *Journal of*
901 *Volcanology and Geothermal Research*, **175**, 334-354.
902 <http://dx.doi.org/10.1016/j.jvolgeores.2008.03.017>
- 903 Giordano, D., Russell, J.K., Dingwell, D.B., 2008, Viscosity of magmatic liquids: A
904 model. *Earth Planet. Sci. Letts.* **271**, 123-134,
- 905 Hammerschmidt, K., Döbel, R. & Friedrichsen, H., 1992. Implication of ⁴⁰Ar/³⁹Ar
906 dating of Early Tertiary volcanic rocks from the north-Chilean
907 Precordillera, *Tectonophysics*, **202**, 55-81.
- 908 Hampel, A., 2002. The migration history of the Nazca Ridge along the Peruvian
909 active margin: a re-evaluation, *Earth and Planetary Science Letters*, **203**,
910 665-679, [http://dx.doi.org/10.1016/S0012-821X\(02\)00859-2](http://dx.doi.org/10.1016/S0012-821X(02)00859-2)
- 911 Hildreth, W., 1979, The Bishop Tuff: evidence for the origin of compositional
912 zonation in silicic magma chambers. *Geological Society of America Special*
913 *Papers*, **180**, 43-76
- 914 Hildreth, W., 1981. Gradients in silicic magma chambers: implications for
915 lithospheric magmatism, *Journal of Geophysical Research: Solid Earth*
916 (1978–2012), **86**, 10153-10192.
- 917 Hildreth, W., & Wilson, C. J., 2007, Compositional zoning of the Bishop Tuff,
918 *Journal of Petrology*, **48**, 951-999,
919 <http://dx.doi.org/10.1093/petrology/egm007>

920 Huber, C., Bachmann, O. & Dufek, J., 2012. Crystal-poor versus crystal-rich
921 ignimbrites: A competition between stirring and reactivation, *Geology*, **40**,
922 115-118, <http://dx.doi.org/10.1130/G32425.1>

923 Isacks, B.L., 1988. Uplift of the central Andean plateau and bending of the
924 Bolivian orocline, *Journal of Geophysical Research: Solid Earth (1978–*
925 *2012)*, **93**, 3211-3231.

926 Jordan, T., Nester, P., Blanco, N., Hoke, G., Davila, F. & Tomlinson, A., 2010. Uplift
927 of the Altiplano - Puna plateau: A view from the west, *Tectonics*, **29**,
928 <http://dx.doi.org/10.1029/2010TC002661>

929 Jordán, T.E., Isacks, B.L., Allmendinger, R.W., Brewer, J.A., Ramos, V.A. & Ando,
930 C.J., 1983. Andean tectonics related to geometry of subducted Nazca plate,
931 *Geological Society of America Bulletin*, **94**, 341-361.

932 Kobberger, G., & Schmincke, H. U., 1999, Deposition of rheomorphic ignimbrite D
933 (Mogán Formation), Gran Canaria, Canary Islands, Spain, *Bulletin of*
934 *Volcanology*, **60**, 465-485

935 Lahsen, A., 1982, Upper Cenozoic volcanism and tectonism in the Andes of
936 northern Chile. *Earth-Science Reviews*, **18**, 285-302.

937 Lindsay, J., Schmitt, A., Trumbull, R., De Silva, S., Siebel, W. & Emmermann, R.,
938 2001. Magmatic evolution of the La Pacana caldera system, Central Andes,
939 Chile: compositional variation of two cogenetic, large-volume felsic
940 ignimbrites, *Journal of Petrology*, **42**, 459-486.

941 Lipman, P., Dungan, M. & Bachmann, O., 1997. Comagmatic granophyric granite
942 in the Fish Canyon Tuff, Colorado: implications for magma-chamber
943 processes during a large ash-flow eruption, *Geology*, **25**, 915-918.

944 Lipman, P.W. & Bachmann, O., 2015. Ignimbrites to batholiths: Integrating
945 perspectives from geological, geophysical, and geochronological data,
946 *Geosphere*, **11**, 705-743, <http://dx.doi.org/10.1130/GES01091.1>

947 Mamani, M., Wörner, G. & Sempere, T., 2010. Geochemical variations in igneous
948 rocks of the Central Andean orocline (13 S to 18 S): Tracing crustal
949 thickening and magma generation through time and space, *Geological*
950 *Society of America Bulletin*, **122**, 162-182,
951 <http://dx.doi.org/10.1130/B26538.1>

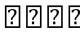
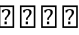
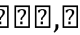
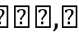
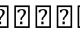
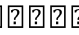
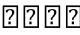
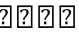








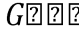
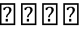
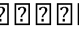
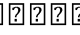
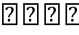
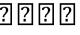
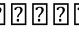
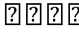
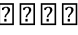






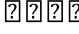
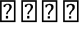
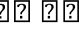
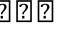










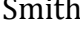

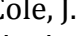
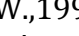
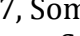
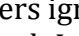
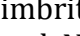
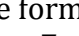
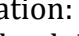

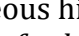
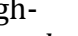



952 Marti, J., Diez - Gil, J. & Ortiz, R., 1991. Conduction model for the thermal
953 influence of lithic clasts in mixtures of hot gases and ejecta, *Journal of*
954 *Geophysical Research: Solid Earth (1978–2012)*, **96**, 21879-21885.

955 Martinod, J., Husson, L., Roperch, P., Guillaume, B. & Espurt, N., 2010. Horizontal
956 subduction zones, convergence velocity and the building of the Andes,
957 *Earth and Planetary Science Letters*, **299**, 299-309,
958 <http://dx.doi.org/10.1016/j.epsl.2010.09.010>

959 Mattinson, J.M., 2005. Zircon U–Pb chemical abrasion (“CA-TIMS”) method:
960 combined annealing and multi-step partial dissolution analysis for
961 improved precision and accuracy of zircon ages, *Chemical Geology*, **220**,
962 47-66. <http://dx.doi.org/10.1016/j.chemgeo.2005.03.011>

963 Maughan, L.L., Christiansen, E.H., Best, M.G., Gromme, C.S., Deino, A.L. & Tingey,
964 D.G., 2002. The Oligocene Lund Tuff, Great Basin, USA: a very large
965 volume monotonous intermediate, *Journal of Volcanology and Geothermal*
966 *Research*, **113**, 129-157, [http://dx.doi.org/10.1016/S0377-](http://dx.doi.org/10.1016/S0377-0273(01)00256-6)
967 [0273\(01\)00256-6](http://dx.doi.org/10.1016/S0377-0273(01)00256-6)

- 968 McDonald, I. & Viljoen, K., 2006. Platinum-group element geochemistry of mantle
969 eclogites: a reconnaissance study of xenoliths from the Orapa kimberlite,
970 Botswana, *Applied Earth Science: Transactions of the Institutions of Mining
971 and Metallurgy: Section B*, **115**, 81-93,
972 <http://dx.doi.org/10.1179/174327506X138904>
- 973 McLean, N., Bowring, J. & Bowring, S., 2011. An algorithm for U - Pb isotope
974 dilution data reduction and uncertainty propagation, *Geochemistry,
975 Geophysics, Geosystems*, **12**, <http://dx.doi.org/10.1029/2010GC003478>
- 976 McLean, N.M., Condon, D.J., Schoene, B. & Bowring, S.A., 2015. Evaluating
977 uncertainties in the calibration of isotopic reference materials and multi-
978 element isotopic tracers (EARTHTIME Tracer Calibration Part II),
979 *Geochimica et Cosmochimica Acta*, **164**, 481-501,
980 <http://dx.doi.org/10.1016/j.gca.2015.02.040>
- 981 Miller, C.F. & Wark, D.A., 2008. Supervolcanoes and their explosive
982 supereruptions, *Elements*, **4**, 11-15,
983 <http://dx.doi.org/10.2113/GSELEMENTS.4.1.11>
- 984 Montgomery and Brandon, 2002, Topographic controls on erosion rates in
985 tectonically active mountain ranges, *Earth and Planetary Science Letters*,
986 **201**, 481-489, [http://dx.doi.org/10.1016/S0012-821X\(02\)00725-2](http://dx.doi.org/10.1016/S0012-821X(02)00725-2)
- 987 Muller, L. D., 1977. "Density determination." Physical methods in determinative
988 mineralogy, *Academic Press, London*, 663-673.
- 989 Muñoz, N. & Charrier, R., 1996. Uplift of the western border of the Altiplano on a
990 west-vergent thrust system, northern Chile, *Journal of South American
991 Earth Sciences*, **9**, 171-181.
- 992 Parmigiani, A., Huber, C. & Bachmann, O., 2014. Mush microphysics and the
993 reactivation of crystal - rich magma reservoirs, *Journal of Geophysical
994 Research: Solid Earth*, **119**, 6308-6322,
995 <http://dx.doi.org/10.1002/2014JB011124>
- 996 Peterson, D.W., 1979. Significance of the flattening of pumice fragments in ash-
997 flow tuffs, *Geological Society of America Special Papers*, **180**, 195-204.
- 998 Polacci, M., Papale, P. & Rosi, M., 2001. Textural heterogeneities in pumices from
999 the climactic eruption of Mount Pinatubo, 15 June 1991, and implications
1000 for magma ascent dynamics, *Bulletin of Volcanology*, **63**, 83-97.
- 1001 Quane, S.L. & Russell, J.K., 2005. Ranking welding intensity in pyroclastic
1002 deposits, *Bulletin of Volcanology*, **67**, 129-143.
- 1003 Riehle, J., Miller, T. & Bailey, R., 1995. Cooling, degassing and compaction of
1004 rhyolitic ash flow tuffs: a computational model, *Bulletin of Volcanology*,
1005 **57**, 319-336.
- 1006 Rosi, M., Landi, P., Polacci, M., Di Muro, A. & Zandomenighi, D., 2004. Role of
1007 conduit shear on ascent of the crystal-rich magma feeding the 800-year-
1008 BP Plinian eruption of Quilotoa Volcano (Ecuador), *Bulletin of
1009 Volcanology*, **66**, 307-321.
- 1010 Russell, J.K. & Quane, S.L., 2005. Rheology of welding: inversion of field
1011 constraints, *Journal of Volcanology and Geothermal Research*, **142**, 173-
1012 191, <http://dx.doi.org/10.1016/j.jvolgeores.2004.10.017>
- 1013 Sahy, D., Condon, D.J., Terry, D.O., Fischer, A.U. & Kuiper, K.F., 2015.
1014 Synchronizing terrestrial and marine records of environmental change
1015 across the Eocene–Oligocene transition, *Earth and Planetary Science
1016 Letters*, **427**, 171-182, <http://dx.doi.org/10.1016/j.epsl.2015.06.057>

- 1017 Salas, R., Kast, R., Montecinos, F., Salas, I., 1966. Geología y Recursos Minerales
1018 del Departamento de Arica. Provincia de Tarapacá. Inst. Invest. Geol., **21**,
1019 130 pp.
- 1020 Scheuber, E. & Gonzalez, G., 1999. Tectonics of the Jurassic - Early Cretaceous
1021 magmatic arc of the north Chilean Coastal Cordillera (22°-26° S): A story
1022 of crustal deformation along a convergent plate boundary, *Tectonics*, **18**,
1023 895-910.
- 1024 Self, S., 2006. The effects and consequences of very large explosive volcanic
1025 eruptions, *Philosophical Transactions of the Royal Society A: Mathematical,*
1026 *Physical and Engineering Sciences*, **364**, 2073-2097,
1027 <http://dx.doi.org/10.1098/rsta.2006.1814>
- 1028                              
- 1029               
- 1030               
- 1031 Smith, T. R., Cole, J. W., 1997, Somers ignimbrite formation: Cretaceous high-
1032 grade ignimbrites from South Island, New Zealand, *Journal of volcanology*
1033 *and geothermal research*, **75**, 39-57
- 1034 Somoza, R., 1998. Updated azca (Farallon)—South America relative motions
1035 during the last 40 My: implications for mountain building in the central
1036 Andean region, *Journal of South American Earth Sciences*, **11**, 211-215.
- 1037 Sparks, R., Francis, P., Hamer, R., Pankhurst, R., O'callaghan, L., Thorpe, R. & Page,
1038 R., 1985. Ignimbrites of the Cerro Galan Caldera, NW Argentina, *Journal of*
1039 *Volcanology and Geothermal Research*, **24**, 205-248.
- 1040 Sparks, R., Tait, S. & Yanev, Y., 1999. Dense welding caused by volatile resorption,
1041 *Journal of the Geological Society*, **156**, 217-225.
- 1042 Steven, T.A. & Lipman, P.W., 1976. Calderas of the San Juan Volcanic Field,
1043 Southwestern Colorado: Eighteen Major Ash-flow Tuff Sheets Were
1044 Deposited and Perhaps as Many Related Calderas Developed During
1045 Emplacement of an Underlying Shallow Batholith in Late Oligocene Time,
1046 edn, *Geological Survey Professional Paper*, **958**, US Government Printing
1047 Office.
- 1048 Tobar, A., Kast, R.F. & Salas, I., 1968. *Carta geologica de Chile. Cuadrangulo*
1049 *Camaraca y Azapa, provincia de Tarapaca*, Inst. Invest. Geol., Carta Geol.
1050 Chile, **19-20**, 13 p
- 1051 Tosdal, R.M., Farrar, E. & Clark, A.H., 1981. K-Ar Geochronology of the Late
1052 Cenozoic volcanic rocks of the Cordillera Occidental, southernmost Perú,
1053 *Journal of Volcanology and Geothermal Research*, **10**, 157-173.
- 1054 Vallance, J.W., 2005. Volcanic debris flows. in *Debris-flow Hazards and Related*
1055 *Phenomena*, 247-274
- 1056 Vazquez, J. A., Reid, M. R., 2004, Probing the accumulation history of the
1057 voluminous Toba magma. *Science*, **305**, 991-994
- 1058 Vogel, S., Vila, T., 1980. Cuadrángulos Arica y Poconchile. *Región de Tarapacá.*
1059 *Instituto de Investigaciones Geológicas*, Carta Geológica de Chile, **35**, 24 p.
- 1060 Wendt, I. & Carl, C., 1991. The statistical distribution of the mean squared
1061 weighted deviation, *Chemical Geology: Isotope Geoscience Section*, **86**, 275-
1062 285.
- 1063 Whitney, J.A. & Stormer, J.C., 1985. Mineralogy, petrology, and magmatic
1064 conditions from the Fish Canyon Tuff, central San Juan volcanic field,
1065 Colorado, *Journal of Petrology*, **26**, 726-762.

- 1066 Willcock, M. A. W., Cas, R. A. F., Giordano, G., & Morelli, C., 2013, The eruption,
1067 pyroclastic flow behaviour, and caldera in-filling processes of the
1068 extremely large volume (> 1290km³), intra-to extra-caldera, Permian Ora
1069 (Ignimbrite) Formation, Southern Alps, Italy. *Journal of Volcanology and*
1070 *Geothermal Research*, **265**, 102-126,
1071 <http://dx.doi.org/10.1016/j.jvolgeores.2013.08.012>
1072 Wilson, C. J., Hildreth, W., 1997, The Bishop Tuff: new insights from eruptive
1073 stratigraphy, *The Journal of Geology*, **105**, 407-440.
1074 Wotzlaw, J.-F., Schaltegger, U., Frick, D.A., Dungan, M.A., Gerdes, A. & Günther, D.,
1075 2013. Tracking the evolution of large-volume silicic magma reservoirs
1076 from assembly to supereruption, *Geology*, **41**, 867-870,
1077 <http://dx.doi.org/10.1130/G34366.1>
1078 Wotzlaw, J.F., Decou, A., von Eynatten, H., Wörner, G. & Frei, D., 2011. Jurassic to
1079 Palaeogene tectono - magmatic evolution of northern Chile and adjacent
1080 Bolivia from detrital zircon U - Pb geochronology and heavy mineral
1081 provenance, *Terra Nova*, **23**, 399-406, [http://dx.doi.org/10.1111/j.1365-](http://dx.doi.org/10.1111/j.1365-3121.2011.01025.x)
1082 [3121.2011.01025.x](http://dx.doi.org/10.1111/j.1365-3121.2011.01025.x)
1083 Wotzlaw, J. F., Bindeman, I. N., Watts, K. E., Schmitt, A. K., Caricchi, L., Schaltegger,
1084 U., 2014. Linking rapid magma reservoir assembly and eruption trigger
1085 mechanisms at evolved Yellowstone-type supervolcanoes, *Geology*, **42**,
1086 807-810, <http://dx.doi.org/10.1130/G35979.1>
1087 Wright, H.M., Folkes, C.B., Cas, R.A. & Cashman, K.V., 2011. Heterogeneous pumice
1088 populations in the 2.08-Ma Cerro Galán Ignimbrite: implications for
1089 magma recharge and ascent preceding a large-volume silicic eruption,
1090 *Bulletin of volcanology*, **73**, 1513-1533.
1091 <http://dx.doi.org/10.1007/s00445-011-0525-5>
1092 Wörner, G., Hammerschmidt, K., Henjes-Kunst, F., Lezaun, J. & Wilke, H., 2000.
1093 Geochronology (⁴⁰Ar/³⁹Ar, K-Ar and He-exposure ages) of Cenozoic
1094 magmatic rocks from Northern Chile (18-22° S): implications for
1095 magmatism and tectonic evolution of the central Andes, *Revista geológica*
1096 *de Chile*, **27**, 205-240.
1097 Wörner, G., Uhlig, D., Kohler, I. & Seyfried, H., 2002. Evolution of the West Andean
1098 Escarpment at 18 S (N. Chile) during the last 25 Ma: uplift, erosion and
1099 collapse through time, *Tectonophysics*, **345**, 183-198,
1100 [http://dx.doi.org/10.1016/S0040-1951\(01\)00212-8](http://dx.doi.org/10.1016/S0040-1951(01)00212-8)
1101
1102

1103

1104

1105 **Figure Captions**

1106 **Fig. 1. (a)** The Andean Cordillera along the west coast of South America. The box
1107 indicates the part of the Central Andes shown in Figure 1b. **(b)** The estimated
1108 extent of the early Miocene ignimbrites in northernmost Chile and southernmost

1109 Peru. (c) Part of the Central Andes in southern Peru and northern Chile,
1110 indicating the five geomorphological units after Garcia et al. (2011). (d)
1111 Geological map of the study area in northernmost Chile that is based on our own
1112 observations and the 'Arica Map' by Garcia et al. (2004). The geology of Peru is
1113 not shown.

1114

1115 **Fig. 2.** Field photography of the Molinos section, located in the northern wall of
1116 the Lluta Quebrada, Central Basin, indicating the Cardones, Molinos and Oxaya
1117 ignimbrites with intercalated sediments.

1118

1119 **Fig. 3.** (a) Correlation of general stratigraphic columns of the Molinos section
1120 (Fig. 2) and the nine drill holes. (b) Two cross-sections across and along the
1121 western Andean Slope. The Oxaya Formation is gently folded in the Huaylillas
1122 anticline.

1123

1124 **Fig. 4.** (a) Photograph of a crystal-rich pumice clast (CRP); (b) a crystal-poor
1125 pumice clast (CPP); (c) mingling of a CRP and CPP. (d) Petrographic
1126 photograph (PPL) of bulk ignimbrite at the top and CRP at the base of the image.
1127 The dotted lines indicate single fractured crystals. (e) Petrographic photograph
1128 (PPL) of CPP; (f) a microdiorite clasts; (g) a band of small crystal fragments of a
1129 heavily fractured plagioclase crystal in a CRP that is outlined by the dotted lines.
1130 (h) Petrographic photograph of a microdiorite clast with entrained quartz
1131 crystals. (N.B. non-petrographic images are of wet rock.)

1132

1133 **Fig. 5. (a)** Detailed stratigraphic columns of the Cardones ignimbrite in the nine
1134 drill holes, correlating the different units and subunits across the holes. Note that
1135 hole 1 is shown twice. **(b)** Vertical profiles of pumice clasts throughout seven
1136 different holes. Stack plots show the absolute numbers of crystal-rich (blue) and
1137 crystal-poor (red) pumice clasts and the black line indicates the pumice
1138 intersection percentage. **(c)** Vertical profiles showing the absolute number of
1139 lithic clasts (dashed green) and the lithic intersection percentage (black). Pie-
1140 diagrams indicate the total number of lithic clasts and the fraction of each lithic
1141 type per subunit. **(d)** Vertical profiles of the average aspect ratios of crystal-rich
1142 and crystal-poor pumice per 25 meters.

1143

1144 **Fig. 6.** Density of bulk rock (open diamonds) and of crystal-rich pumice (CRP -
1145 closed diamonds) for the Cardones ignimbrite, drill hole 1. The dashed line
1146 shows the fiamme aspect ratio profile for CRPs.

1147

1148 **Fig. 7.** Representative photographs of the Cardones ignimbrite; **(a-d)** subunits in
1149 unit 1; **(e)** and unit 2. Scale bars are 50mm and photographs are made of wet
1150 rock.

1151

1152 **Fig. 8.** Summary plot of ranked $^{206}\text{Pb}/^{238}\text{U}$ dates for the Oxaya Formation, based
1153 on the data of supplementary material. The weighted mean $^{206}\text{Pb}/^{238}\text{U}$ age with
1154 its analytical uncertainty and MSDW of each sample is given as well.

1155

1156 **Fig. 9. (a)-(e)** major and trace element plots for the Cardones, Molinos and Oxaya
1157 ignimbrite based on the data in supplementary material. The light gray-shaded

1158 areas show the chemistry for crystal-rich (CRP) and crystal-poor (CPP) pumice
1159 clasts in the Cardones ignimbrite. The dark shaded areas indicate the more
1160 limited chemical range for the Cardones bulk ignimbrite. (f) Spider diagram for
1161 representative samples, indicating the negative Eu anomaly and the MREE
1162 minima for all ignimbrites. (g) Vertical chemistry profiles for the Cardones
1163 ignimbrite; and (h) the Molinos and Oxaya ignimbrites.

1164

1165 **Table captions.**

1166 **Table 1.** Thickness of the Cardones ignimbrite per drill hole. The "larger than"
1167 sign means part of that specific unit has been eroded

1168

1169 **Table 2.** Characteristics of the Cardones ignimbrite presented per unit. CRP and
1170 CPP stand for crystal rich pumice clasts and crystal poor pumice clast,
1171 respectively. The symbol \bar{x} is used for average. IP_{juv} and IP_{lit} are the percentile
1172 intersection thickness for juvenile and lithic clasts, respectively.

1173

1174 **Table 3.** Representative major and trace element composition measured via ICP-
1175 OES and ICP-MS

Table 1. Thickness of the Cardones ignimbrite in meters

Hole	Total (m)	Unit 1 subunit 1	Unit 1 subunit 2	Unit 1 subunit 3	Unit 1 subunit 4	Unit 2
M	~300	unkown	unkown	unkown	unkown	unkown
7	468	0	110	250	110	-
4	578	0	150	330	100	-
2	691	0	170	410	110	-
1	>911	130	200	550	>40	-
5	>426	0	200	>230	eroded	-
6	>778	0	250	350	~130	> 50 m
9	816	0	30	215	210	360
3	>473	0	30	>440	eroded	-
10	>64	0	0	>74	eroded	-

Table 2. Summary of the main characteristics of the Cardones ignimbrite per unit

Unit	Subunit	drill holes	Thickness	Colour	crystallinity bulk rock	Bulk density kg/m ³	IP _{juv}	CRP/CPP	aspect ratios CRP	aspect ratios CPP	IP _{lit}	Size and type composition clasts
2	-	6, 9	50 - 360 m	pinkish white/ grey	38 - 46%	-	4.40%	>95/<5	top half: 1 - 11.9 \bar{x} = 3.9, n = 161 base half: 0.6 - 6.3 \bar{x} = 2.4, n = 161	-	7.0%	1 - 100 mm top half: dacite, rhyolite base half: andesite, dacite, rhyolite
1	4	7, 4, 2, 1, 6,7,9	100 - 210 m	pinkish white/ white	~36%	1900	10%	>99/<1	0.5 - 8.6 \bar{x} = 3.4, n = 161	-	4.7%	65% rhyolite, dacite (2-132 mm, \bar{x} = 23) <20% granite (1-50 mm \bar{x} = 19) <5% andesite (1-18 mm \bar{x} = 6.9)
1	3	all cores	550-250 m	light reddish browy	36 - 51%	2300 ± 100	3.10%	85/15	0.2 - 23 \bar{x} = 5.4, n = 1399 top half: \bar{x} = 6.4 base half: \bar{x} = 4.2	1.25 - 30 \bar{x} = 7.2, n = 492	0.2%	1 - 100 mm 50% granite 20% andesite 20% rhyolite, dacite
1	2	7, 4, 2, 1, 5, 6, 9, 3	30-250 m	light reddish brown/ grey	47 - 50%	2300 ± 100	3%	67.33	0.3 - 11 \bar{x} = 4.0, n = 269	1.4 - 14 \bar{x} = 5.3, n = 141	4.3%	60% andesite (1-59 mm, \bar{x} = 5.2) 30% granite (2-56 mm, \bar{x} = 11.1) 10% others
1	1	1	130 m	grey/pinkish white	23 - 30%	top: 2400 base: 1900	1%	50/50	0.5 - 10.5 \bar{x} = 3.9, n = 65	1.5 - 13 \bar{x} = 4.9, n = 16	2.1%	3 - 15 mm, lithics have alteration haloes 50% andesite 40% granite 10% others

<i>Table 3. Representative major and trace element composition of the Oxaya Formation</i>							
Member	Cardones	Cardones	Cardones	Cardones	Cardones	Molinos	Oxaya Lower unit
Sample	130038P	130040P	130020P	130015-MD	130018	707P	703
Core:	1	1	1	1	1	7	7
type	CRP	CRP	CPP	Microdiorite	Bulk	Pumice	Bulk
SiO ₂	70.13	71.33	70.31	60.31	75.53	74.26	74.69
TiO ₂	0.27	0.14	0.18	0.61	0.16	0.16	0.12
Al ₂ O ₃	13.32	12.30	12.47	16.54	11.88	12.18	11.91
Fe ₂ O ₃	2.39	1.19	1.38	6.32	1.42	0.88	0.83
MnO	0.07	0.06	0.05	0.07	0.07	0.06	0.07
MgO	0.70	0.70	0.39	0.81	0.43	0.26	0.42
CaO	2.15	2.10	1.44	4.12	1.48	0.93	0.69
Na ₂ O	3.17	2.56	3.14	4.21	2.79	3.24	2.81
K ₂ O	3.85	4.61	4.93	2.55	3.63	3.86	3.93
P ₂ O ₅	0.08	0.02	0.03	0.19	0.03	0.03	0.01
volatiles	3.13	4.13	4.85	3.67	1.78	3.93	4.17
Total	99.26	99.15	99.17	99.42	99.20	99.79	99.66
V	37.94	17.39	20.32	82.55	19.65	21.11	16.81
Cr	27.93	1.70	10.07	1.92	9.35	0.86	3.18
Co	4.42	1.88	2.51	15.58	2.34	0.88	0.28
Ni	41.48	4.12	2.47	1.86	16.37	8.41	2.58
Cu	23.16	13.35	8.06	39.01	7.71	11.89	11.82
Zn	57.49	12.71	10.57	51.34	17.47	71.00	29.67
Ga	14.58	12.87	13.04	18.73	11.91	10.89	13.36
Rb	113.74	151.23	144.46	101.91	132.69	127.76	162.19
Sr	243.84	125.16	166.69	249.36	162.65	107.92	47.78
Y	12.91	16.91	13.52	16.15	13.83	11.61	20.13
Zr	125.82	75.16	77.57	126.71	68.36	75.36	69.68
Nb	7.99	10.21	9.82	7.57	7.56	8.50	15.56
Mo	2.10	2.39	1.99	1.12	1.45	1.98	2.35
Sn	5.18	2.22	2.85	1.59	3.22	1.23	2.24
Cs	8.74	5.61	5.70	4.23	4.69	4.66	8.70
Ba	899.52	546.50	611.73	286.27	723.04	1103.03	313.43
La	33.20	25.81	27.66	25.87	28.17	30.92	24.45
Ce	59.35	47.29	47.04	47.51	50.32	54.78	48.81
Pr	5.98	5.13	5.14	5.38	5.20	5.84	5.41
Nd	18.33	16.09	15.95	19.36	16.00	18.64	17.57
Sm	2.97	3.01	2.88	3.94	2.94	2.89	3.60
Eu	0.73	0.50	0.53	0.81	0.54	0.57	0.32
Gd	2.54	2.65	2.44	3.02	2.38	2.08	2.71
Tb	0.31	0.37	0.32	0.42	0.32	0.28	0.44

Dy	1.86	2.26	1.92	2.42	1.98	1.72	2.82
Ho	0.36	0.46	0.38	0.47	0.39	0.35	0.55
Er	1.13	1.41	1.19	1.50	1.17	1.15	1.83
Tm	0.19	0.25	0.20	0.25	0.22	0.18	0.31
Yb	1.38	1.77	1.48	1.81	1.51	1.39	2.18
Lu	0.23	0.31	0.25	0.25	0.25	0.23	0.34
Hf	3.44	2.49	2.54	3.22	2.13	2.33	2.56
Ta	0.85	1.31	1.16	0.52	1.02	0.90	1.46
Pb	18.90	20.78	20.63	20.07	19.73	19.52	21.64
Th	12.71	16.91	15.26	4.52	15.62	5.88	5.88
U	3.71	4.85	5.16	3.74	3.96	2.85	4.22

Oxaya
Upper unit
701
7
Bulk
74.88
0.22
13.07
1.26
0.06
0.20
1.03
3.56
4.75
0.04
0.69
99.75
25.98
2.04
1.65
1.83
19.28
22.96
13.11
126.75
127.70
14.95
125.37
11.47
0.95
0.62
2.53
1020.44
39.88
68.49
7.37
23.21
3.85
0.66
2.68
0.38

2.24
0.42
1.44
0.22
1.66
0.26
3.44
0.92
18.74
10.09
2.42

Figure 1

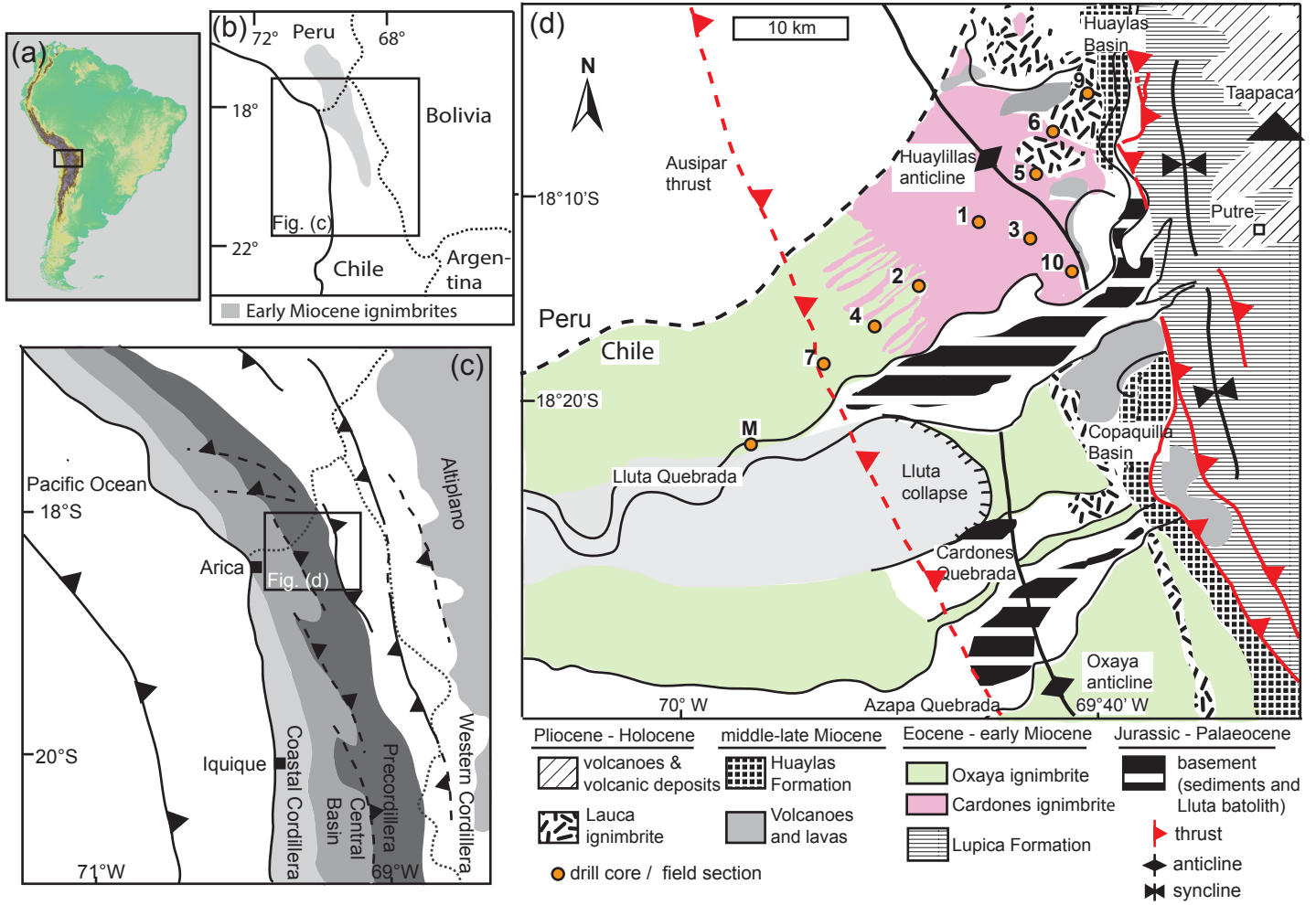


Figure 2

[Click here to download Figure Fig. 2. Molinos section.pdf](#)

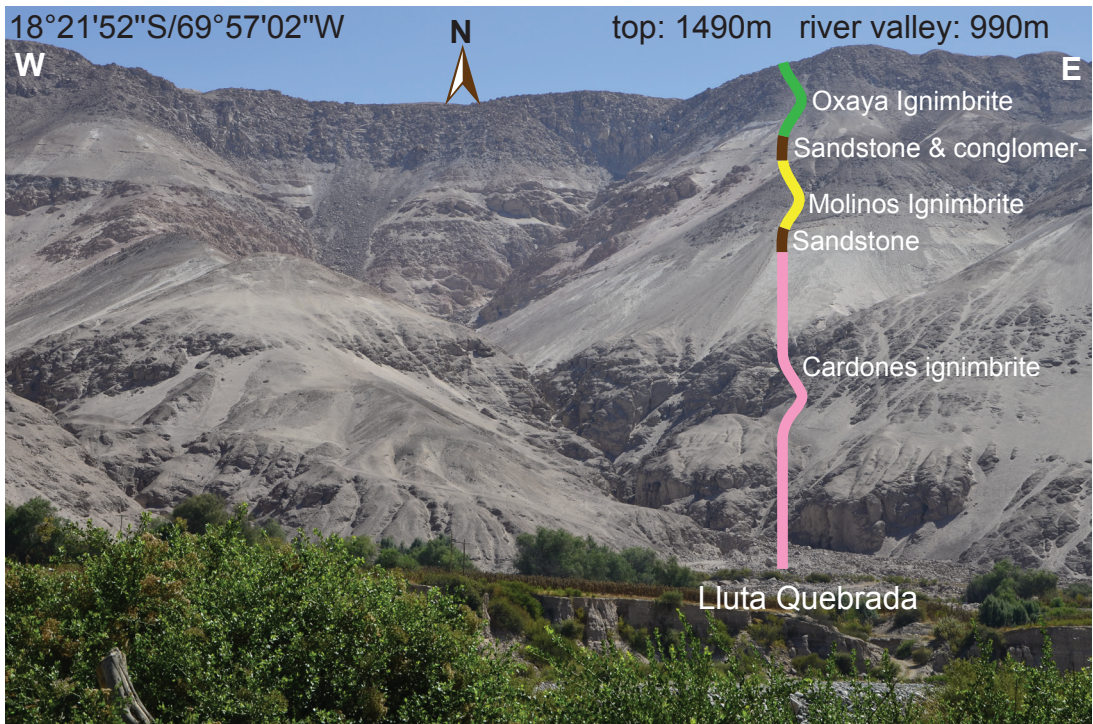
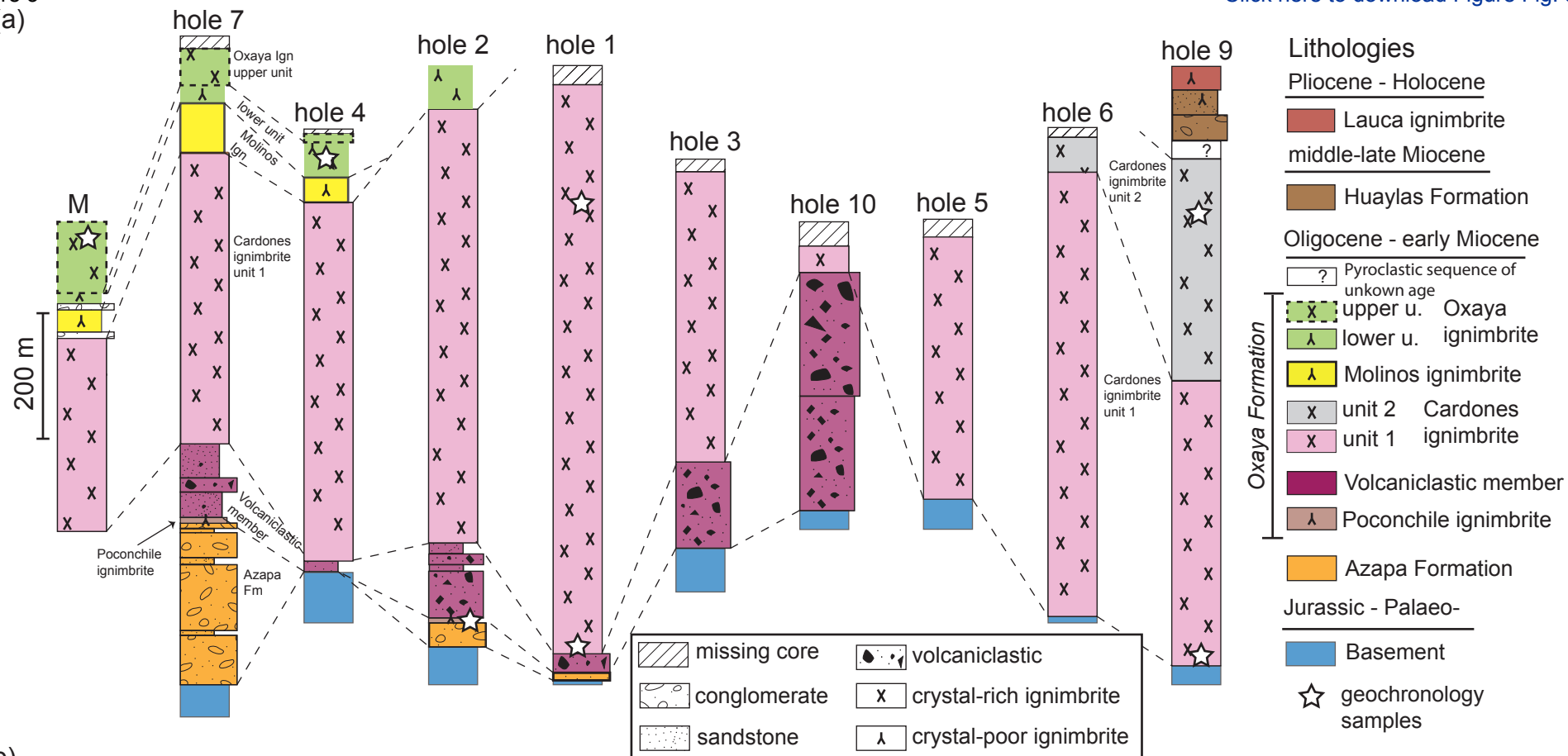


Figure 3

(a)



(b)

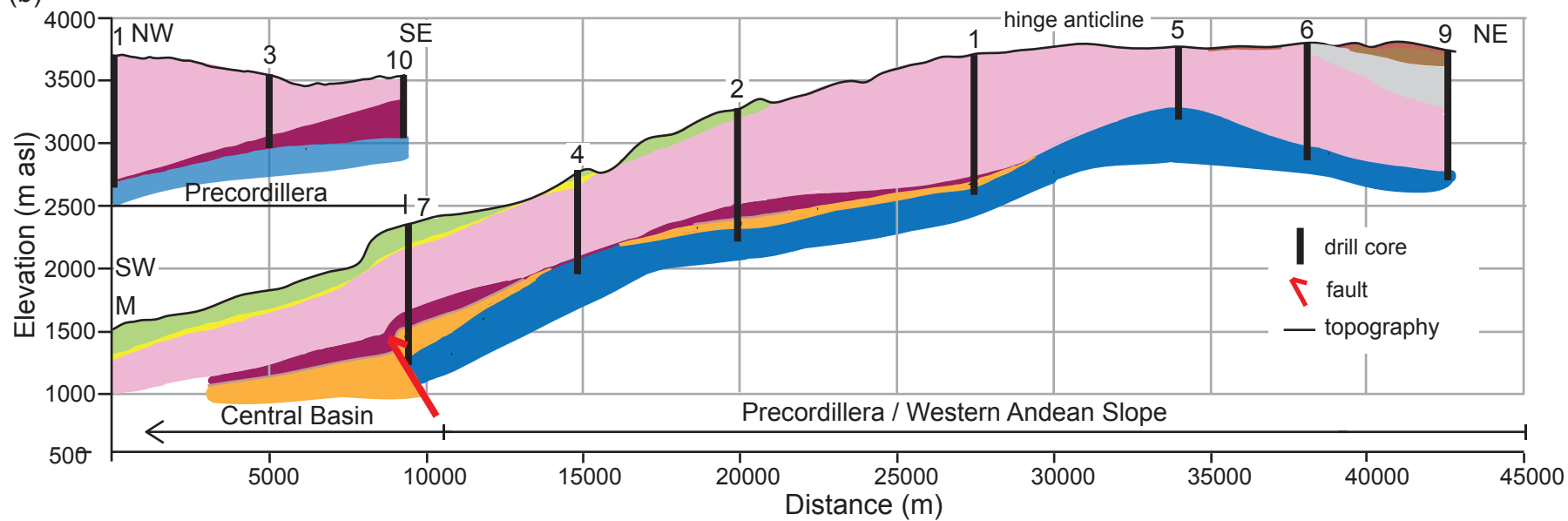


Figure 4

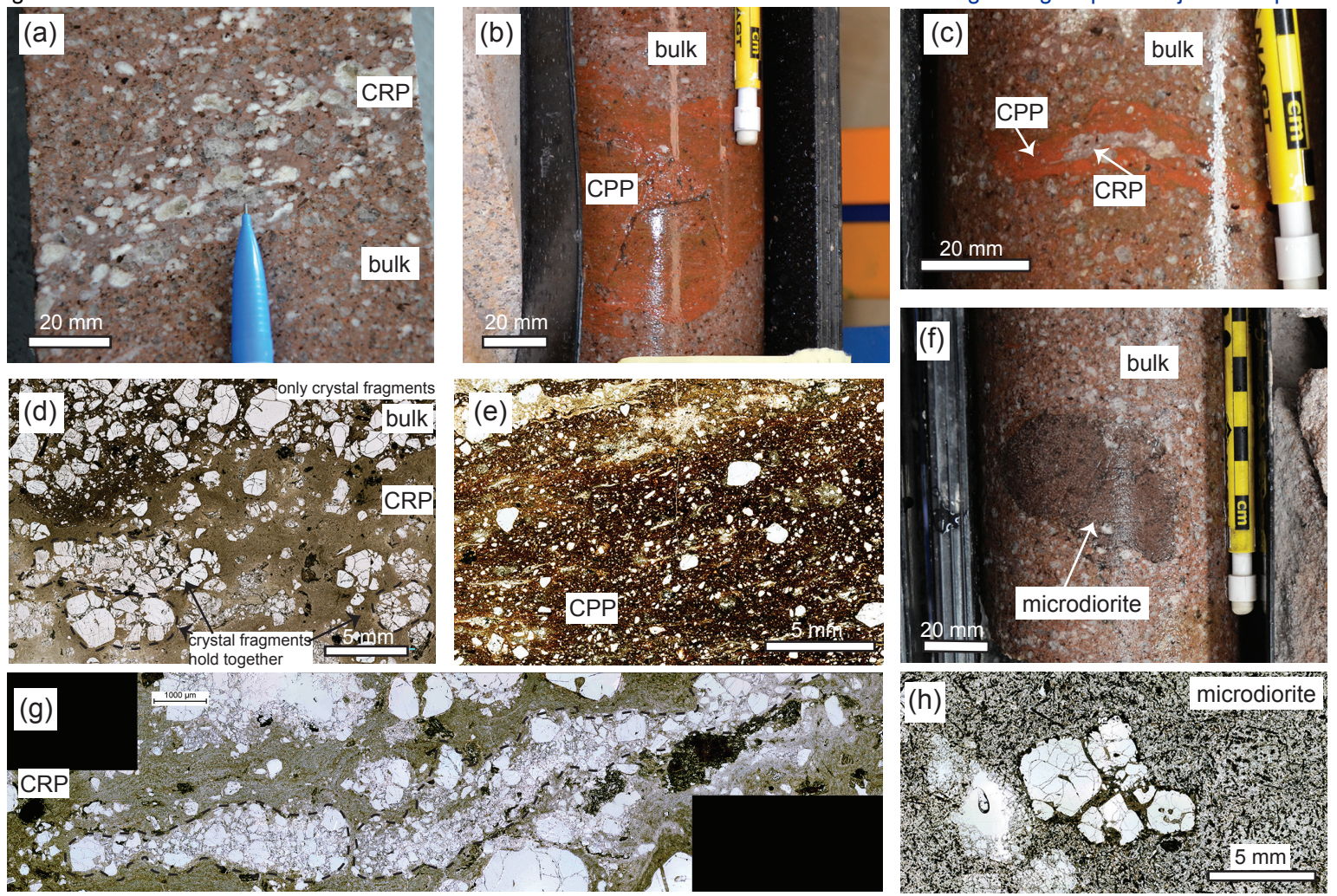


Figure 5 Stratigraphic columns Cardones ignimbrite

Click here to download Figure Fig. 5. Cardones drill core.pdf

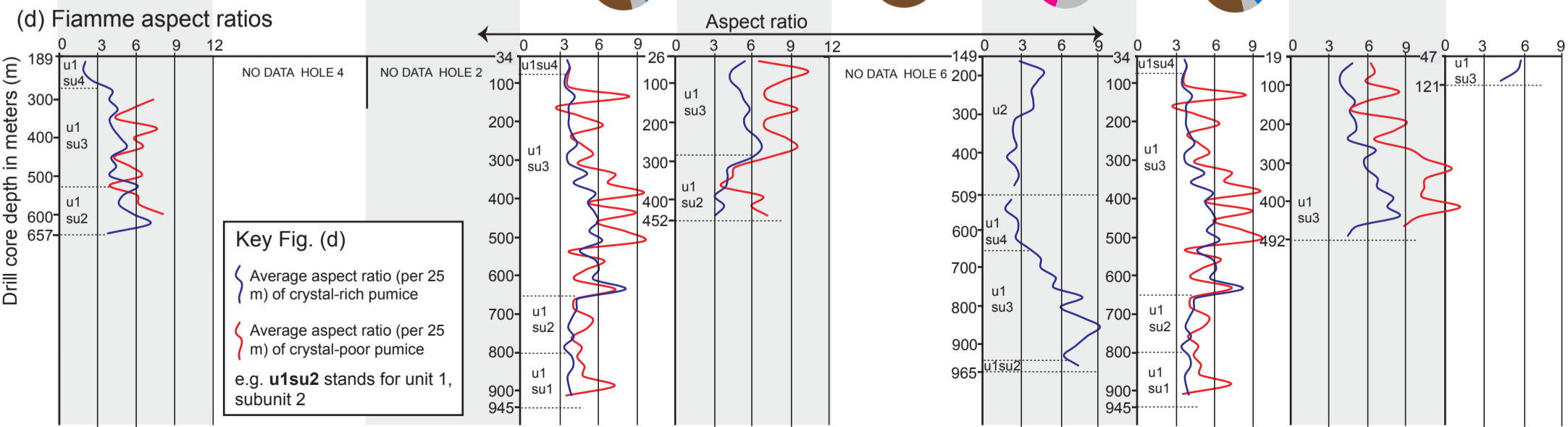
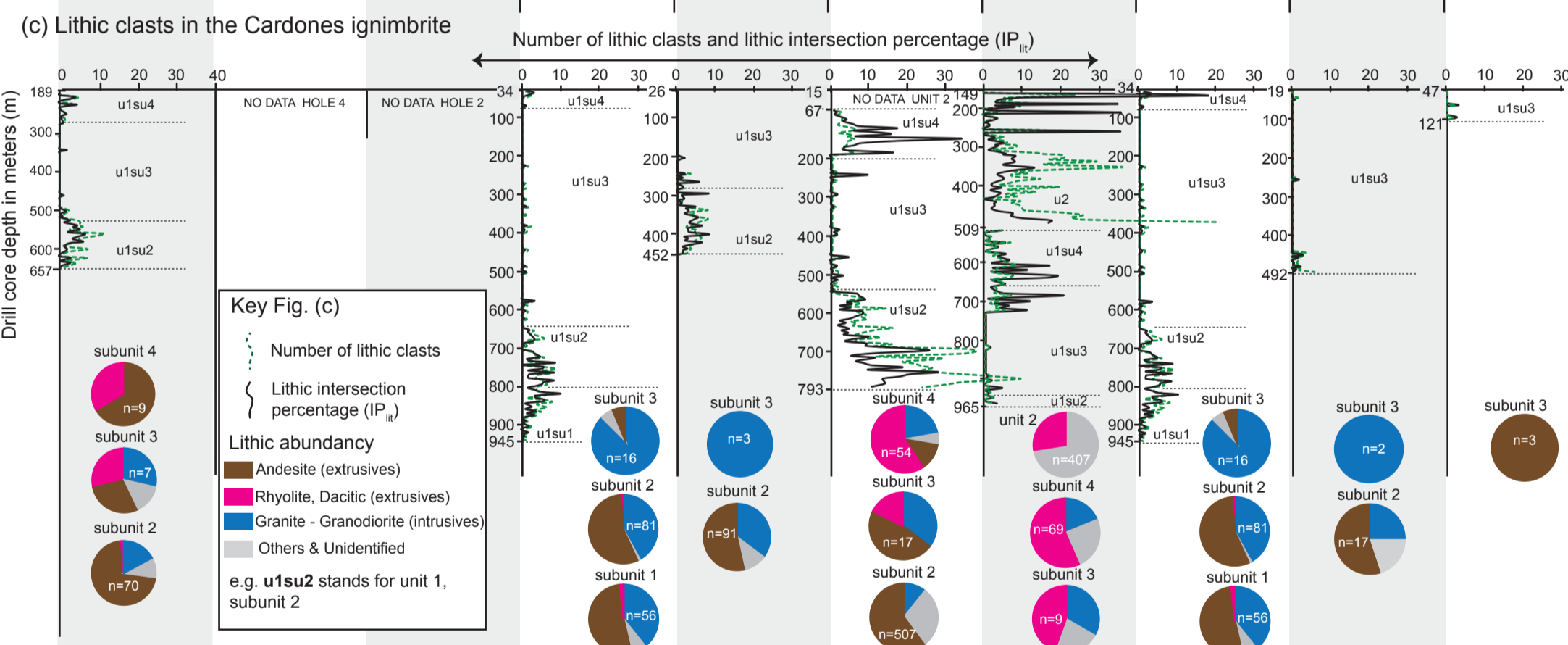
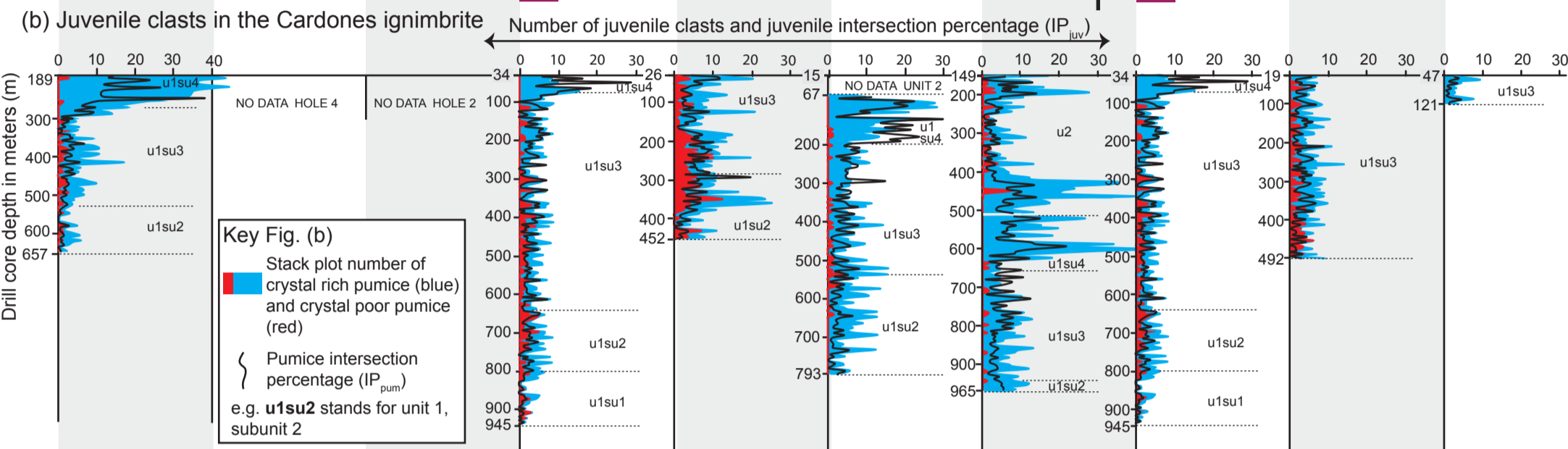
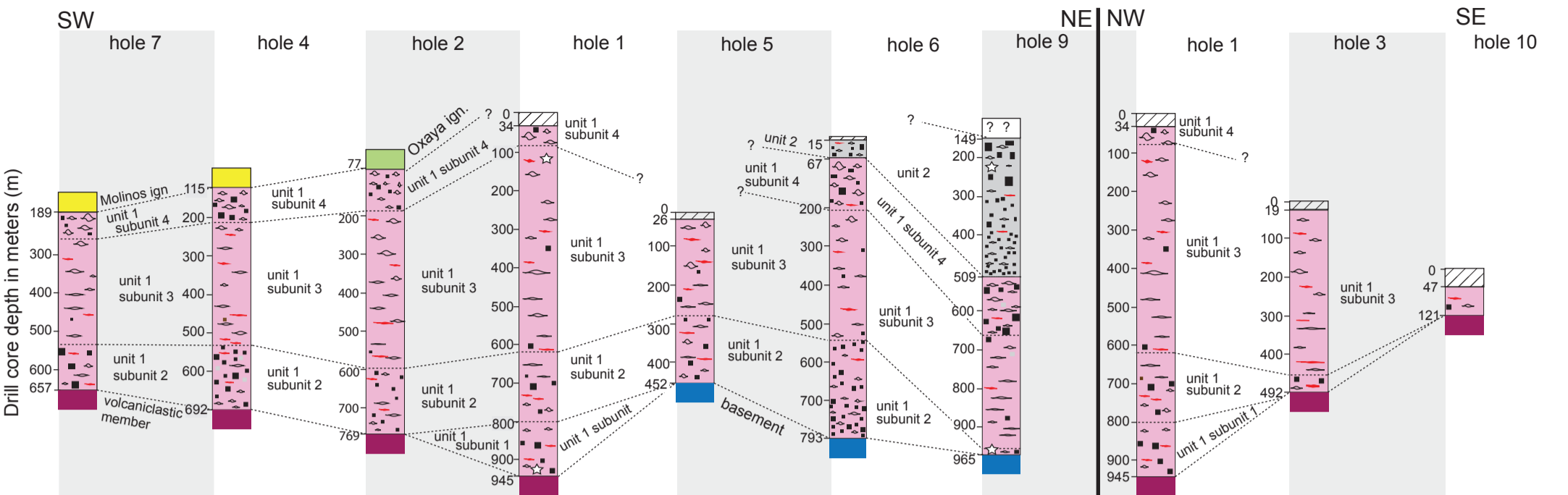
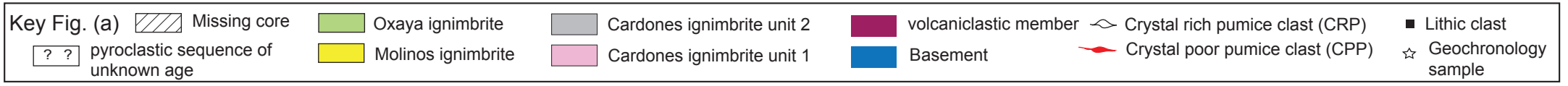


Figure 6

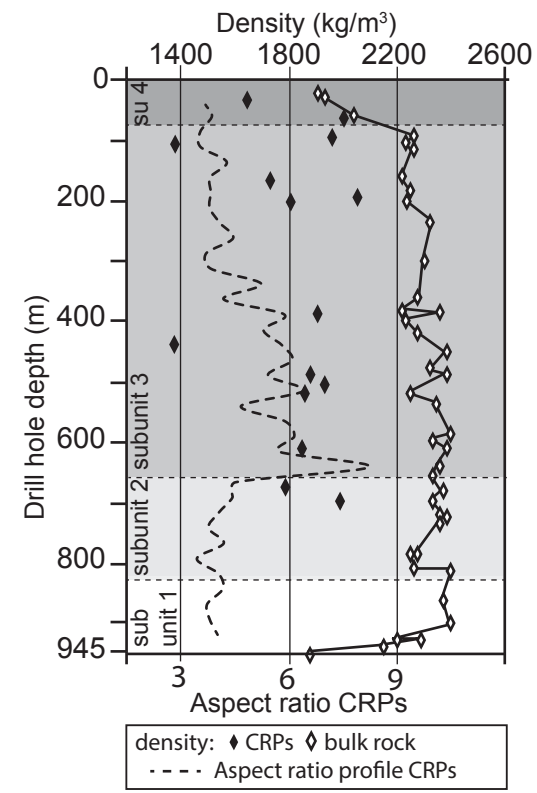
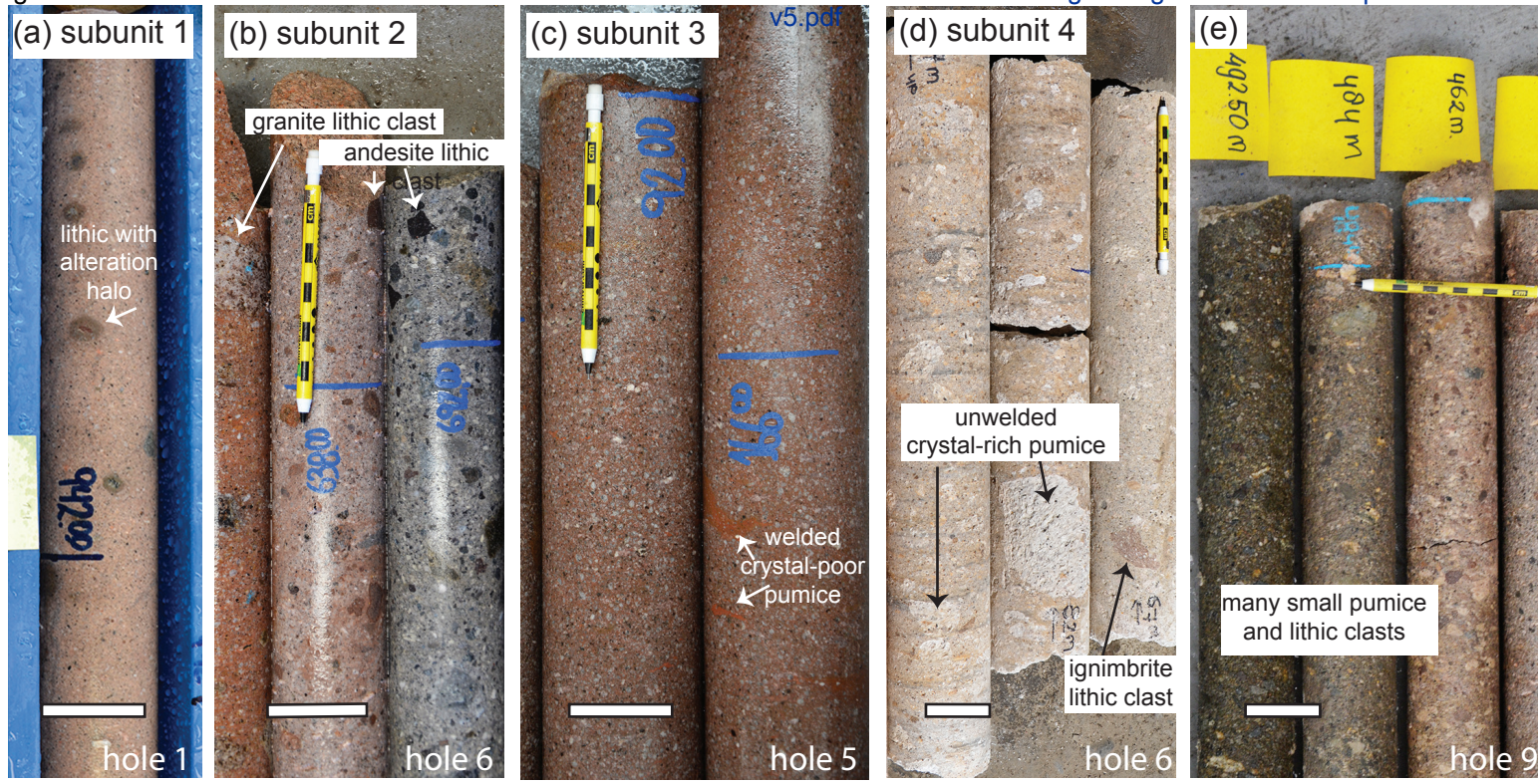
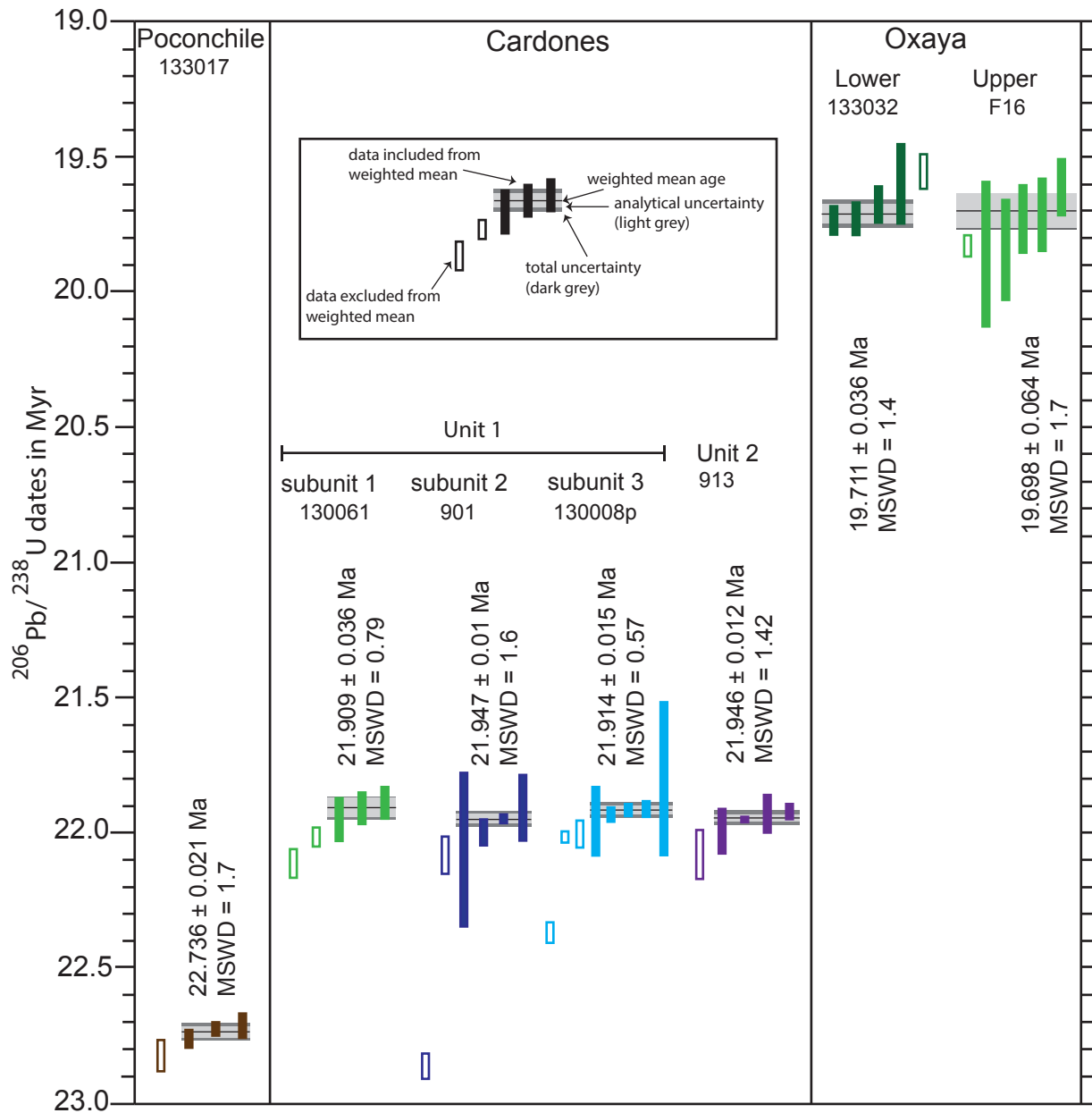
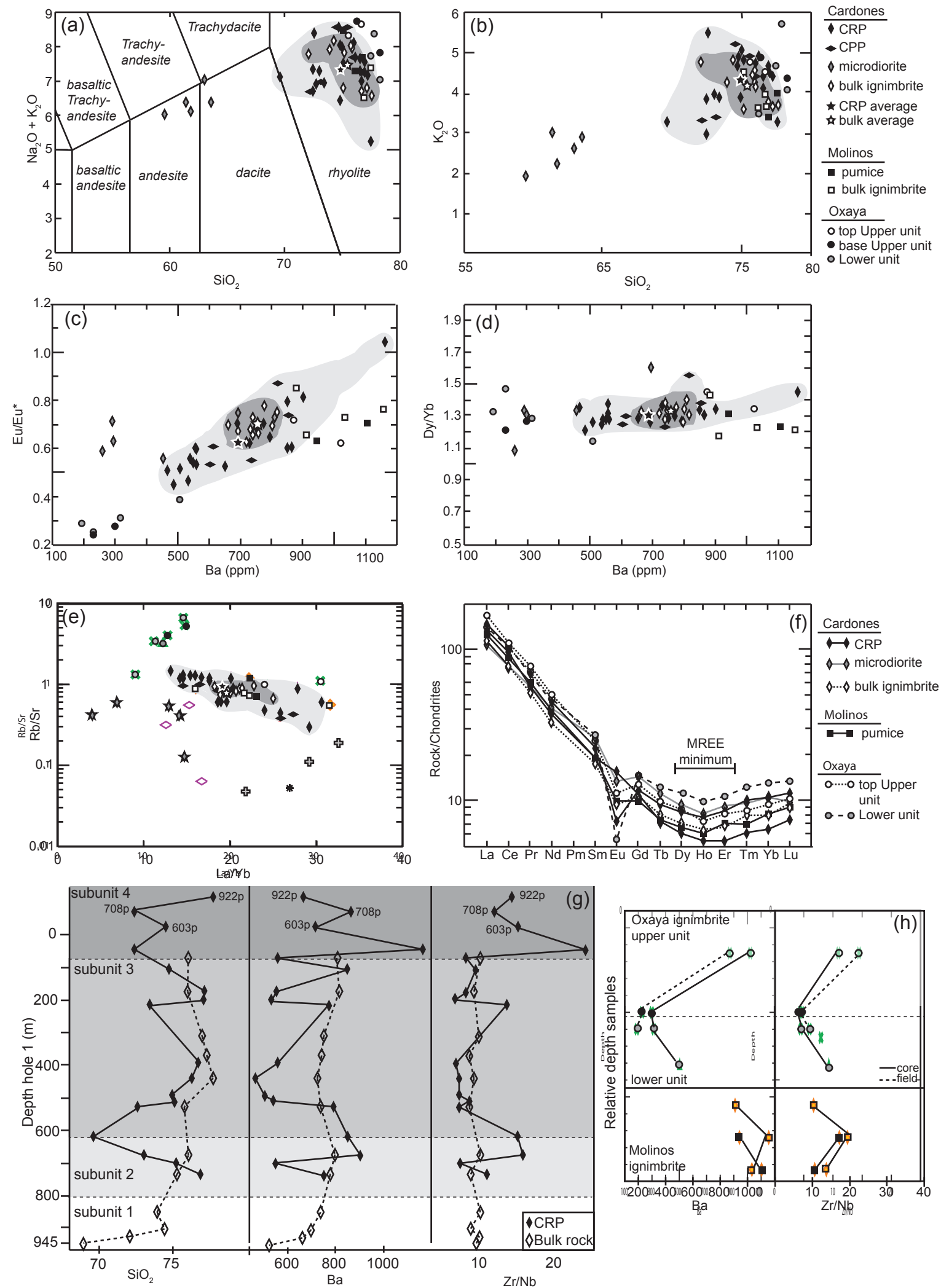


Figure 7

[Click here to download Figure Fig. 7. core-interval pictures v5.pdf](#)









[Click here to access/download](#)

Dataset

Supplementary Material Table S1.csv





[Click here to access/download](#)

Dataset

Supplementary Material Table S2.csv

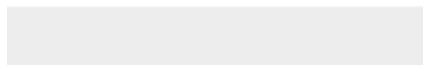




[Click here to access/download](#)

Dataset

Supplementary Material Table S3.csv





[Click here to access/download](#)

Supplementary material (not datasets)
Supplementary material.docx

